Measurement of the normal polarisation variable, P_0^y , in a $^2H(e, e'\vec{n})$ experiment

Andrew M. Scott

Presented as a Thesis for the Degree of Doctor of Philosophy

Department of Physics and Astronomy,

University of Glasgow,

March 2002.

ProQuest LLC.
789 East Eisenhower Parkway
P.O. Box 1346
Ann Arbor, MI 48106 – 1346

Abstract

The High Acceptance Recoil Polarimeter (HARP) is a new polarimeter detector which is based on the recoil principle, using liquid hydrogen as an analyser. With the analysing power, A_y well known for *n-p* and *p-p* scattering, the asymmetry from the incoming nucleon flux and the normal polarisation variable, P_0^y can be determined in a $^2H(e,e'\vec{n})$ reaction. The $^2H(e,e'\vec{n})$ experiment which was performed at NIKHEF, Amsterdam which utilised HARP as means to detect the polarisation of the neutron took place late in 1997.

This thesis documents my involvement in the building and testing of this new detector system, my participation in the development of the data-acquisition software and in a commissioning experiment which took place at NIKHEF in November 1996 involving HARP. My work at ISN Grenoble on the analysis of the wire chamber information from the commissioning experiment is also documented.

An overview of the HARP detector and its components are described and their performance under experimental conditions are documented. In addition, the experimental hall at NIKHEF, Emin, is also described.

This thesis also describes the running of the $^2\mathrm{H}(e, e'\vec{n})$ experiment, the set-up at the experimental hall at NIKHEF and the problems encountered during this experiment involving the failure of the electron beam and the wire chambers of the HARP detector. A novel analysis method to extract as much information as possible in the absence of wire chamber data and with the reduced beam time of the experiment is presented where a value of 0.03 for P_0^y is found.

Declaration

The experiment was performed at the National Institute for Nuclear Physics and High Energy Physics (NIKHEF). I participated fully in the execution of the experiment. The data presented in this thesis was obtained by the HARP collaboration, consisting of the Nuclear Physics groups at the University of Glasgow, NIKHEF, University of Utrecht, ISN Grenoble and University of Regina. The analysis and interpretation of the experimental data is my own work. This thesis was composed by myself.

Andrew M. Scott

Acknowledgements

During my work on this thesis I was fortunate enough to come into contact with a huge number of people, all of whom I would like to thank for making these past years what they were. Although there are too many people to list individually, I'd like to specifically thank the following:

I would like to thank my supervisor, Dr. David Ireland, and the rest of the Nuclear Physics Group at Glasgow University for their help, advice and support.

I would also like to express thanks for the abundant hospitality I received from everyone I met at NIKHEF, Universiteit Utrecht and ISN Grenoble. I was always made to feel at home and have fond memories of visiting these institutes.

A big thanks goes to the HARP collaboration, to everyone who took part in the experiment and to all the technicians involved, every one of whom shed blood, sweat and tears to keep HARP and the EMIN hall operational.

I reserve a very special thank you for Dr. Thomas Bauer and Dr. Eric Voutier who devoted so much of their time to help and guide me through

my studies whilst abroad and to whom I will always be indebted. I should also take this opportunity to thank their families for putting up with my demands on Thomas' and Eric's time.

I would like to thank the Engineering and Physical Sciences Research Council and to the Glasgow University Nuclear Physics Group for providing financial support and travel expenses during my time as a student.

Finally I have to thank Margaret, my wife, who endured so much during my work.

Contents

1 Introduction 1

2 Theory and Review 7

2.1 The Deuteron 8

2.2 The formalism of electron scattering 11

2.2.1 Electron-Nucleus scattering formalism 11

2.2.2 Spin observables 17

2.2.3 Nucleon recoil polarisation 19

2.3 Electron accelerators 22

2.4 Neutron detection 24

2.4.1 The time-of-flight method 24

2.4.2 The recoil proton detection method 26

2.4.3 Measuring neutron polarisation with a polarimeter 28

3 High Acceptance Recoil Polarimeter 31

3.1 Overview of the detector 32

3.1.1 The liquid hydrogen converter 35
3.1.2 The wire-chambers 38
3.1.3 Scintillator telescopes 42
3.1.4 Charged particle tagger 45
3.2 The HARP trigger 46
3.3 The gas safety system 49
3.4 Phases of construction 49

4 Commissioning Experiment **51**
4.1 Data acquisition 53
4.1.1 Data acquisition software 53
4.2 Evaluation of the HARP wire-chambers 54
4.2.1 Further testing of the wire-chambers 56
4.2.2 Re-evaluation of the wire-chambers 60
4.3 Conclusion 60

5 The ^{2}H$(e, e'\vec{n})$ Experimental Set-up **63**
5.1 The electron accelerator facility 64
5.2 The QDQ spectrometer 67
5.3 The deuterium target 68
5.4 The data acquisition system and
electronics 68
5.5 Overview of kinematics 71
5.6 Summary of experiment 71

6 Data Analysis and Results **75**

6.1 QDQ analysis 77

6.2 HARP analysis 78

6.2.1 Position calibration 79

6.2.2 Energy calibration 81

6.2.3 Event selection 97

6.3 Coincidence analysis 99

6.3.1 Timing coincidence 100

6.3.2 The recoil proton scattering angle 106

6.3.3 Correction for background 109

6.3.4 Calculation of P_0^y 110

6.3.5 Results of analysis 111

7 Conclusion and the Future of HARP **114**

List of Figures

2.1 Experimental cross-sections 10

2.2 The electron scattering process 12

2.3 Contributions to the ^{2}H$(e, e'N)$ cross-section 16

2.4 Theoretical plot for P_0^y (Arenhovel) 22

2.5 The time-of-flight method 25

2.6 Measuring polarisation variables using the TOF method . . . 26

2.7 The RPD technique 27

2.8 The analysing power of LH_2 for neutron scattering 29

3.1 The HARP Detector 34

3.2 The LH_2 vessel 37

3.3 The LH_2 system 37

3.4 Field lines inside a MWPC 38

3.5 Exploded view of a wire-chamber 41

3.6 The scintillator telescope 44

3.7 The 3 scintillator layers 45

3.8 The charged particle tagger layout 46

3.9 HARP trigger logic layout 48

3.10 The mean-timer 48

4.1 The data acquisition set-up for HARP 55

4.2 Testing the wire-chambers 55

4.3 Illustration of hot-wires in wire-chamber data 57

4.4 Reconstruction of secondary scattering angle 59

5.1 Experimental set-up 65

5.2 The Amsterdam Pulse Stretcher (AmPS) 66

5.3 The QDQ spectrometer 69

5.4 The internal workings of the QDQ spectrometer 69

5.5 The liquid deuterium target 70

5.6 The coincidence trigger logic 72

6.1 Determination of the nucleon energy entering HARP from QDQ analysis 78

6.2 The hit position in a scintillator bar 80

6.3 Position calibration results 83

6.4 Light output as a function of incident energy 85

6.5 2 proton coincidences in the scintillator arrays 92

6.6 Angular correlation in $(p, 2p)$ scattering events 93

6.7 Geometry of $(p, 2p)$ events within HARP 94

6.8 The interaction vertex within the converter 95

6.9 The raw HARP-QDQ timing coincidence 101

6.10 The HARP-QDQ timing coincidence 102

6.11 The 'walk' effect 104

6.12 The HARP-QDQ timing peak resolution 105

6.13 Energy deposit vs. scattering angle 107

6.14 Reconstruction of secondary scattering angle from scintillator data 109

6.15 Asymmetry seen in HARP for incoming neutrons 111

6.16 P_0^y result 112

List of Tables

3.1 HARP MWPC wire characteristics 40

3.2 Differences between HARP Phase I and Phase II 50

4.1 HARP MWPC efficiency measurements (laboratory testing) . 56

4.2 HARP MWPC efficiency measurements (commissioning experiment) 59

4.3 HARP MWPC efficiency measurements (re-evaluation testing) 61

5.1 Overview of kinematics for the ^{2}H$(e, e'\vec{n})$ experiment 74

6.1 HARP MWPC position calibration parameters 82

6.2 Calculated attenuation constants 89

Chapter 1

Introduction

During the most part of the 19^{th} century, all matter was considered to be composed of combinations of different kinds of indivisible atoms. With the discovery of X-rays, the radioactivity of Uranium and finally the discovery of the electron in the later years of the 19^{th} century, this picture changed to suggest the sub-structure of the atom and so formed the basis of belief that atoms consisted of a mixture composed of positive matter and negatively charged electrons.

In 1911, Rutherford [Ruth11] showed that the positive charge of the atom was concentrated in a small dense nucleus surrounded by a cloud of electrons. Rutherford later showed in 1919 that in fact the positive nucleus contained positively charged particles which he named protons [Ruth19]. It was still assumed at this time that the observed mass (A) and charge (Z) of the atom was due to a composition of A protons and (A-Z) electrons with a further Z electrons orbitting the nucleus.

Chadwick's discovery of the neutron in 1932 [Chad32] dispelled this picture of the nucleus and led to the understanding that the neutron, proton and electron were the elementary particles from which all matter was made.

The measurement of the magnetic moment of the proton, μ_p, by Frisch and Stern [Fris33] in 1933 which showed a significant deviation from that predicted indicated that the proton was not an elementary particle, but itself had further sub-structure. Alvarez and Bloch later measured the magnetic moment of the neutron [Alva40], confirming that the neutron also had sub-structure.

The discovery of pions and muons in the late 1940s and early 1950s [Pow50] provided proof to Yukawa's prediction [Yuka35] of the existence of a fundamental particle with mass that could be used to explain some aspects of the exchange forces between nucleons.

Pion-nucleon cross-section predictions were unable to match experimental data until deep inelastic scattering experiments in the 1960's and early 1970's led to the discovery that nucleons and pions are in fact systems of quarks and antiquarks bound by a force due to the exchange of gluons.

Quantum Chromodynamics (QCD) theory describes the interaction between quarks and gluons and is currently believed to hold the fundamental quantum-field description of the dominant forces acting within the nucleus. QCD theory works well on a small scale, but the calculations become unworkable at low energies (at length scales of more than a few fm) where quark-gluon theory cannot be treated pertubatively.

To advance nuclear physics further, it is therefore necessary to describe the internal structure of the nucleon using phenomenological models whose parameters are fixed with continuing experimental data. In the field of nuclear physics, the atomic nucleus is instead described as a system composed of protons and neutrons which interact through the exchange of mesons. This approach works best in few-body systems such as ^{2}H and ^{3}He where the wave-functions can be described precisely. In heavier nuclei this is not so straight-forward and models based on approximations have to be used.

Current models of nuclei can accurately reproduce various properties of

the nucleus (such as energy levels, spins and parities of ground states etc.), especially in few-body nuclei, but there are still aspects of experimental data which are not yet fully explained. Differences between theory and what is observed experimentally are believed to be (amongst other effects) due to sub-nucleonic effects such as Δ resonances (the first excited state of a nucleon) and the re-scattering and exchange processes which occur during the reaction process (known as final state interactions or FSI). It is therefore important to measure observables which are sensitive to these effects, in order to determine their relative importance.

The study of such observables requires a well understood target environment so that unambiguous results can be determined from experimental data. The deuteron is a good choice in which to study these observables; it is the simplest compound nucleus consisting of a proton and a neutron with spin one and isospin zero and is the ideal starting point to observe and understand these sub-nucleonic effects.

Many different experimental methods have been employed in this search to understand and parameterise these models of which just one method is the scattering of electrons on target nuclei. The probing of the nucleus with electrons has always played an outstanding part in the study of the structure and dynamics of the nucleus [Boff95]. This is the case because the electro-magnetic interaction is well known and weak enough to allow lowest order perturbation treatment. Due to the weakness of this interaction, the cross-sections in electro-magnetic reactions are much smaller than those in

purely hadronic reactions. However, recent advances in both target and beam technologies, which have allowed higher target densities and luminosity of beams, have compensated for this.

In a bid to further understand the physics of nucleii there are certain quantities that can be measured that allow the exploration of different aspects of current theory; one such observable being polarisation. Under certain (kinematical) conditions, the measurement of the spin polarisation of the ejected neutron in a plane normal to its momentum direction [1], henceforth referred to as the normal polarisation variable, in a ^{2}H$(e, e'\vec{n})$ reaction is sensitive to FSI effects. Through this measurement we will greatly extend our knowledge of the $(e, e'N)$ reaction mechanism. An experiment to measure the normal polarisation variable in a ^{2}H$(e, e'\vec{n})$ reaction took place in November 1997 using the EMIN facility at the Nationaal Instituut voor Kernfysica en Hoge-Energiefysica (NIKHEF), Amsterdam, The Netherlands.

In chapter 2 of this thesis a more in-depth review of the deuteron is presented as well as an overview of the formalism of the ^{2}H$(e, e'\vec{n})$ reaction. In addition, the polarisation observables of such a reaction are discussed as are the details of how such observables are measured. The new detector, HARP, is detailed in chapter 3 with its performance in a commissioning run given in the following chapter. The ^{2}H$(e, e'\vec{n})$ experiment set-up is then covered in chapter 5 with the experimental hall and remaining apparatus

[1] this is the normal direction perpendicular to the plane containing the scattered electron and neutron.

described. Finally the analysis, results and conclusion to the experiment are given in chapters 6 and 7.

Chapter 2

Theory and Review

In this chapter the physics of the deuteron is summarised in section 2.1 before a review of the physics involved in electron scattering experiments and, in particular, the theory relevent to the $^2\mathrm{H}(e, e'\vec{n})$ experiment. An overview of the advances of electron scattering facilities are presented in section 2.3 and finally in section 2.4, techniques for measuring nucleon polarisation are discussed.

2.1 The Deuteron

Electromagnetic and real-photon experiments on the deuteron have played a key role in the development of our understanding of the deuteron's properties.

The deuteron is significant in the study of nuclear physics because it provides a starting point to the understanding of the nucleon-nucleon interaction. The bound two nucleon system has no discrete excited states (and therefore the inter-nucleon force is spin and isospin dependent) and its static properties (such as binding energy, magnetic dipole moment and electric quadrupole moment which are well-known) have been measured experimentally since the earliest days of its study [Chad32] [Rabi40].

The deuteron is the simplest nuclear system to be studied theoretically: its wave-function can be calculated exactly by solving the Schrödinger equation for a realistic nucleon-nucleon potential and the interaction of the two nucleon system is well understood.

The deuteron is therefore the ideal nuclear system to study theoretically and experimentally: it can be described reasonably well by theory and

so provides a basis for modelling heavier nuclei which are not yet so well understood.

Much experimental evidence has been gained from experiments with the deuteron using electromagentic probes [Schr91] [Bern81] [Quin88] which have concentrated on extracting the differential cross-sections as a function of the transferred energy $\mathbf{q}$ and missing momentum $\mathbf{p_m}$ and the determination of the associated structure functions.

However, the standard theory of the nuclear reaction in light nuclei such as the deuteron, even after including Meson Exchange Currents (MEC), is insufficient to explain some aspects of experimental data (e.g. cross-sections, see figure 2.1) in light of basic nucleon-nucleon dynamics. It is through the study of the deuteron that a more detailed knowledge of these effects, such as isobaric currents (IC) and final state interactions (FSI), will become known.

Discriminating amongst various models using available experimental data is difficult due to the fact that the quasi-elastic response is largely determined by the nuclear momentum distribution and phase space available in the reactions. These quasi-elastic response functions tend to be smooth, broad peaks and it is possible to fit any limited set of data to models of these processes by adjusting only a small number of parameters. In order to unambiguously distinguish between the various models (and thus probe deeper into the physics) one needs to increase the richness of the information measured in the experimental reaction. Experiments which include polarisation degrees of freedom provide this additional information at the cost of

greater experimental and analytical complexity. Polarisation observables are discussed futher in section 2.2.2.

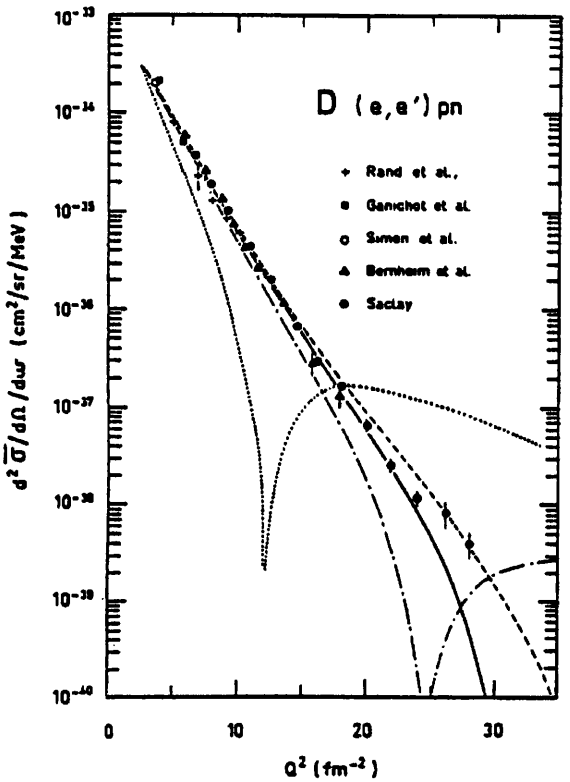

Figure 2.1: *Experimental cross-sections for a wide range of momentum transfer in the $^2H(e,e')pn$ reaction compared to calculations [Auff85] . The dotted curve shows the impulse approximation, the dash-dotted and dashed curves include π and $\pi + \rho$ exchange respectively and the solid curve includes MEC+IC contributions.*

2.2 The formalism of electron scattering

The general formalism of the quasi-elastic ^{2}H$(e, e'N)$ reaction is reviewed in [Boff95]. In this section, the kinematical variables and the cross-section formalism for the ^{2}H$(e, e'N)$ reaction are presented: spin observables are discussed in 2.2.2 after which the recoil polarisation variable is presented.

2.2.1 Electron-Nucleus scattering formalism

A simple description of the $(e, e'N)$ reaction process can be gained by assuming that the interaction between the electron and nucleon takes place through the exchange of a single photon: energy (ω) and momentum ($\mathbf{q}$) are transferred to the nucleus by means of a virtual photon. This virtual photon is assumed to couple to a single nucleon, breaking up the deuteron into a proton and neutron.

In the quasi-elastic ^{2}H$(e, e'N)$ reaction it is assumed that the recoil nucleon is ejected without the creation of other particles such as pions and Δ resonances in the final state.

Figure 2.2 (a) shows the one-photon exchange mechanism: the incoming and scattered electron have four-momenta vectors k_μ and k'_μ respectively. The four-momentum transferred via the virtual photon, q_μ, is the difference of these. Following the convention that the first component of a four-momentum represents the total energy and the other components the momentum, the

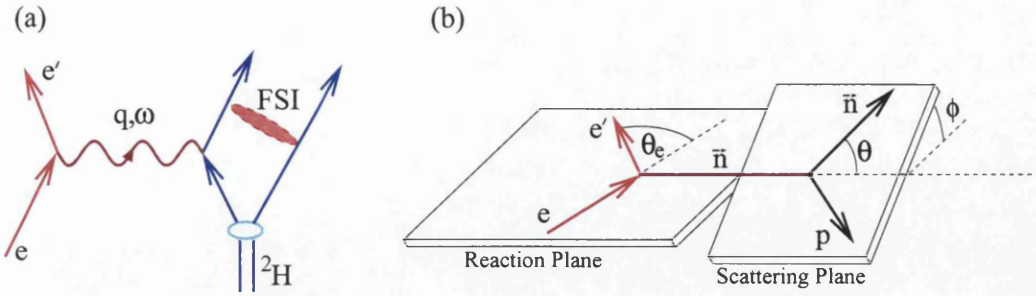

Figure 2.2: (a) *Feynmann diagram showing the one-photon exchange in the* $^2H(e, e'N)$ *reaction* (b) *kinematic planes of electron scattering reaction showing the reaction plane where the one-photon exchange takes places and the secondary scattering plane where the polarised neutron enters HARP and undergoes elastic scattering in the* LH_2 *converter.*

kinematics are defined as:

$$k_\mu = (\epsilon, \mathbf{k}) \tag{2.1}$$

$$k'_\mu = (\epsilon', \mathbf{k}') \tag{2.2}$$

$$q_\mu = (\epsilon - \epsilon', \mathbf{k} - \mathbf{k}') = (\omega, \mathbf{q}) \tag{2.3}$$

Figure 2.2 (b) illustrates the geometry of the $(e, e'N)$ reaction and its kinematics. The angle between the beam and the scattered electron is given by θ_e, the angle between the reaction and scattering planes ϕ and γ_n the angle between the transferred momentum $\mathbf{q}$ and the ejected nucleon.

The electron scattering angle can be deduced from the momentum 3-

vectors:

$$cos\theta_e = \frac{\mathbf{k} \cdot \mathbf{k}'}{|k||k'|} \tag{2.4}$$

An invariant quantity, Q^2, is the energy and momentum exchanged in the scattering process and is defined as:

$$Q^2 = -q_\mu^2 = \mathbf{q^2} - \omega^2 \tag{2.5}$$

Two other useful quantities are the missing energy, E_m, and missing momentum, $\mathbf{p_m}$, which are defined as:

$$E_m = \omega - T_p - T_n \tag{2.6}$$

$$\mathbf{p_m} = \mathbf{q} - \mathbf{p_{recoil}} \tag{2.7}$$

E_m is the energy that is unaccounted for in the experimental measurements. This can be due to the creation of other particles (such as pions) as well as the energy required to break-up the deuteron nucleus[1]. The deuteron binding energy is given as 2.224 MeV, so an experimental measurement of E_m at this value ensures that there are no reaction products unaccounted for.

The five-fold differential cross-section can be written as [Fabi79] [Aren88]:

$$\frac{d^5\sigma}{dk^{lab}d\Omega_e^{lab}d\Omega_{np}^{cm}} = c(\rho_L f_L + \rho_T f_T + \rho_{LT} f_{LT} + \rho_{TT} f_{TT} + h(\rho_{LT}^{'} f_{LT}^{'} + \rho_T^{'} f_T^{'})) \tag{2.8}$$

[1]This can include excitation energies of residual particles, the binding energy of the knocked-out nucleon or the energy required the create new particles.

where the ρ's describe the virtual photon density matrix and are defined as:

$$\begin{aligned}
\rho_L &= q_\mu^2 \frac{\zeta^2}{2\eta} \\
\rho_{LT} &= q_\mu^2 \frac{\zeta}{\eta}\sqrt{(\zeta+\eta)/8} \\
\rho_T &= \frac{1}{2} q_\mu^2 (1+\frac{\zeta}{2\eta}) \\
\rho_{TT} &= -q_\mu^2 \frac{\zeta}{4\eta} \\
\rho'_{LT} &= \frac{1}{2} q_\mu^2 \frac{\zeta}{\sqrt{2\eta}} \\
\rho'_T &= \frac{1}{2} q_\mu^2 \sqrt{(\zeta+\eta)/\eta}
\end{aligned} \tag{2.9}$$

The subscript L and T represent the longitudinal and transverse components respectively (with LT and TT the longitudinal-transverse and transverse-transverse interference components) and c is a kinematical constant proportional to the Mott cross-section. Parameters ζ, η and c are given as:

$$\zeta = \frac{q_\mu^2}{\mathbf{q^2}} \; ; \; \eta = tan^2(\frac{\theta_e^{lab}}{2}) \; ; \; c = \frac{\alpha}{6\pi^2}\frac{k_2}{k_1 q_\mu^4} \tag{2.10}$$

The structure functions are given in terms of T-matrix elements:

$$\begin{aligned}
f_L &= \sum_{smm_d} t_{sm,0m_d} t^*_{sm,0m_d} \\
f_T &= 2\sum_{smm_d} t_{sm,1m_d} t^*_{sm,1m_d} \\
f_{LT} &= 4\Re e \sum_{smm_d} t_{sm,0m_d} t^*_{sm,1m_d} \\
f_{TT} &= 2\sum_{smm_d} t_{sm,-1m_d} t^*_{sm,1m_d} \\
f'_{LT} &= -4\Im m \sum_{smm_d} t_{sm,0m_d} t^*_{sm,0m_d}
\end{aligned} \tag{2.11}$$

with

$$t_{sm,\mu m_d} = -\pi\sqrt{2\alpha p_{np} E E_d / M_d}\langle sm_s|\hat{J}_\mu(\mathbf{q})|\mathbf{m_d}\rangle \tag{2.12}$$

where α denotes the fine structure constant, μ is the photon polarisation, M_d is the deuteron mass and $\hat{J}_\mu$ denotes the charge/current operators.

The final state is characterised by the relative momentum p_{np}, the total spin s and its projection m_s on p_{np}.

If we ignore any final state interactions (FSI) between the ejected nucleon and the residual nucleus, the missing momentum, $\mathbf{p_m}$ is equal to the momentum of the neutron within the nucleus before it is knocked out. This approximation is known as the Plane Wave Impulse Approximation (PWIA).

However other possible effects which include Isobar Currents (where the nucleon is temporarily excited into a resonance state), Meson Exchange Currents (where the virtual photon couples to a virtual meson) and Final State Interactions (during break-up, the nucleons are subject to re-scattering and exchange processes) contribute to the interaction (figure 2.3). A more detailed approach which takes into account FSI, Meson Exchange Currents (MEC) and Isobaric Currents (IC) is required to describe ^{2}H$(e, e'\vec{n})$ cross-section data (e.g. [Bern81], [Auff85]) more accurately. At this 'deeper' level it is desirable to determine the structure functions that together describe the cross-section. Each of these structure functions contribute to the cross-section separately and represents a different combination of nucleon current components, thus probing a different aspect of the reaction.

The differential cross-section can be expressed further such that the

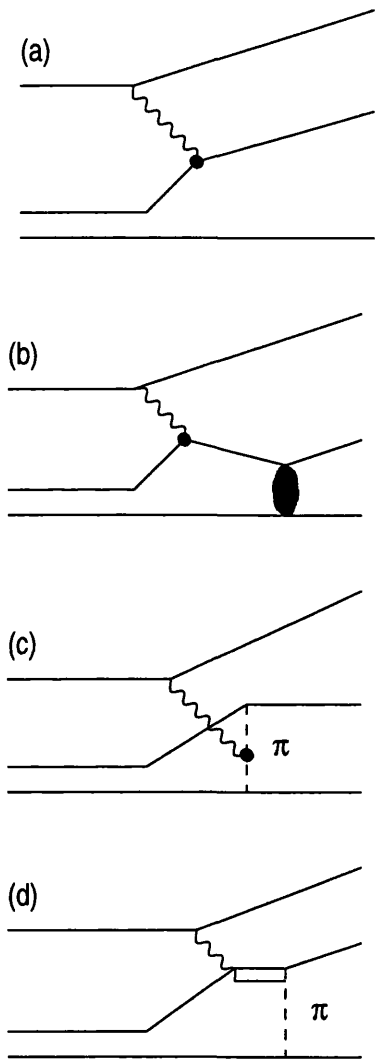

Figure 2.3: *The main processes contributing to the* $^2H(e, e'N)$ *cross-section:* (a) *PWIA e-N scattering*, (b) *final state interactions*, (c) *meson exchanges pair current*, (d) *isobar excitation.*

polarisation dependent parts are separated [Aren88]:

$$\frac{d^5\sigma}{dk^{lab}d\Omega_e^{lab}d\Omega_{np}^{cm}}\mathbf{P} = \mathrm{S}_0(\mathbf{P^0} + h\mathbf{P'}) \tag{2.13}$$

where

$$S_0 = c(\rho_L f_L + \rho_L f_L + \rho_{LT} f_{LT} cos\Phi + \rho_{TT} f_{TT} cos2\Phi) \tag{2.14}$$

where P is the target polarisation, $\mathbf{P^0}$ is the recoil nucleon polarisation, $\mathbf{P'}$ is the electron polarisation, h is the electron beam helicity and c is the same kinematical constant defined previously.

2.2.2 Spin observables

Polarisation is the expectation value of the spin operator over an ensemble of many (non-zero spin) particles. It is conventional to normalise this so that the ensemble of particles with spins all in one direction has a polarisation of unity whereas a completely arbitrary spin orientation has a polarisation of zero. For spin $\frac{1}{2}$ particles such as the neutron and proton, polarisation describes the component of spin (up or down) relative to a particular axis. For an ensemble of such particles, the polarisation in an ideal measurement can be rather generally described by:

$$P = \frac{N_\uparrow - N_\downarrow}{N_\uparrow + N_\downarrow} \tag{2.15}$$

where P is a measure of the polarisation which ranges between (-1,1) and $N_\downarrow$ and $N_\uparrow$ refer to the number of nucleons with their spins aligned up and down respectively.

Measurement of the polarisation of these nucleons involves a spin dependent scattering reaction. This spin dependence of the scattering cross-section is due to the spin-orbit interaction and so it becomes possible to determine the polarisation of nucleons by scattering them in targets which themselves need not be polarised [Aren88] .

Polarisation experiments are a rich source of information on the nucleus; the measurement of polarisation observables enables a more complete determination of the nuclear response than possible with unpolarised experiments alone. These polarisation observables can lead to the extraction of amplitudes which are sensitive to various ingredients of the nuclear model and which would not be visible in the unpolarised case.

The measurement of spin physics in experiments with electromagnetic probes has previously been hampered by technical difficulties, in particular experiments were limited by low duty factor electron beams[2]. With the availability of pulse stretcher rings (such as AmPS at NIKHEF discussed in section 5.1) and higher duty factors of up to ~100%, these experiments are now possible.

[2]Duty Factor is the ratio of pulse duration to the pulse period of a periodic pulse train. A duty factor of 100% corresponds to continuous operations. A low duty factor results primarily in a poor signal/noise ratio.

2.2.3 Nucleon recoil polarisation

For zero beam and target polarisation, the polarisation of the outgoing neutron can be expressed in terms of the functions [Aren88]:

$$p^{\lambda}_{\mu\mu'}(j) = \sum_{sm_s s' m'_s m_d} t_{sm_s,\mu m_d} t^{*}_{s' m'_s \mu' m'_d} \langle s' m'_s | \sigma(j)_\lambda | s m_s \rangle \qquad (2.16)$$

The following symmetry relations

$$(p^{\lambda}_{\mu'\mu})^{*} = (--)^{\lambda} p^{-\lambda}_{\mu\mu'}$$

$$p^{\lambda}_{-\mu'-\mu} = (--)^{1+\lambda+\mu+\mu'} p^{-\lambda}_{\mu'\mu} \qquad (2.17)$$

can then be extensively used in order to derive the following:

$$\frac{d^5\sigma}{dk^{lab} d\Omega^{lab}_e d\Omega^{cm}_{np}} P_{x/z}(j) = c[\rho_{LT} g^{x/z}_{LT} sin\Phi + \rho_{TT} g^{x/z}_{TT} sin2\Phi] \qquad (2.18)$$

$$\frac{d^5\sigma}{dk^{lab} d\Omega^{lab}_e d\Omega^{cm}_{np}} P_{y}(j) = c[\rho_{L} g^{y}_{L}(j) + \rho_{T} g^{y}_{L}(j) + \rho_{LT} g^{y}_{LT}(j) cos\Phi + \rho_{TT} g^{y}_{TT}(j) cos2\Phi] \qquad (2.19)$$

The polarisation structure functions are analagous to f's in equation 2.11 and are defined in terms of the p-functions by:

$$\begin{aligned}
g^{x/y}_{\lambda\mu}(j) &= -\sqrt{2}i \frac{1+\delta_{\lambda+\mu,1}}{1+\delta_{\mu 0}} \Im m(p^{1}_{\lambda\mu}(j) \mp p^{-1}_{\lambda\mu}(j)) \\
g'^{x/y}_{\lambda\mu}(j) &= -\sqrt{2} \frac{1+\delta_{\lambda+\mu,1}}{1+\delta_{\mu 0}} \Re e(p^{1}_{\lambda\mu}(j) \mp p^{-1}_{\lambda\mu}(j)) \\
g^{z}_{\lambda\mu}(j) &= s(1+\delta_{\lambda 0}) \Im m(p^{0}_{\lambda\mu}(j)) \\
g'^{z}_{\lambda\mu}(j) &= s(1+\delta_{\lambda 0}) \Re e(p^{0}_{\lambda\mu}(j))
\end{aligned} \qquad (2.20)$$

The polarisation of the outgoing neutron, $\mathbf{P^0}$, in the ^{2}H$(e, e'\vec{n})$ reaction can be derived from the above and the differential cross-section information in equation 2.13 [Aren88]:.

$$P^{x,z} = \frac{c}{s_0}\left(\rho_{LT} g_{LT}^{x,z} sin\phi + \rho_{TT} g_{TT}^{x,z} sin2\phi\right)$$

$$P^{y} = \frac{c}{s_0}\left(\rho_{L} g_{L}^{y} + \rho_{T} g_{T}^{y} + \rho_{LT} g_{LT}^{y} cos\phi + \rho_{TT} g_{TT}^{y} cos2\phi\right) \qquad (2.21)$$

where c is a kinematical factor, s_0 is the unpolarised cross-section, the $g_{\lambda\mu}$ [3] describe the spin structure functions (given in equation 2.20), the $\rho_{\lambda\mu}$ are the virtual photon density matrix elements and ϕ is the azimuthal angle made by the ejected nucleon around the transferred momentum, $\vec{q}$.

With coplanar kinematics (i.e ϕ=0), it can be seen that all components of the recoil polarisation except P_0^y vanish.

P_0^y can be written as:

$$P^{y} = \frac{c}{s_0}\left(\rho_{L} g_{L}^{y} + \rho_{T} g_{T}^{y} + \rho_{LT} g_{LT}^{y} + \rho_{TT} g_{TT}^{y}\right) \qquad (2.22)$$

If we ignore FSI, then under Watson's theorem, the fifth structure function [4] vanishes in Arenhövel's theoretical calculation for an unpolarised target [5] $g^y \rightarrow 0$ and P_0^y =0. P_0^y for neutrons can be measured in the ^{2}H$(e, e'\vec{n})$ reaction by observing the left-right asymmetry of a secondary scattering reaction involving the recoil neutron. A non zero measurement of P_0^y in the ^{2}H$(e, e'\vec{n})$ reaction would indicate the importance of FSI in the description

[3] The index combinations (00),(11),(01), (-11) refer to L, T, LT and TT respectively.

[4] Whereas the previous four structure functions are directly related to the real part of the interferance between the longitudinal and transverse nuclear current, the fifth is related to the corresponding imaginary part.

[5] Watson's final state theorem states that the reduced t-matrix can be made real for an unpolarised target and hence v_{LT} made real also.

of the nuclear response.

There are a number of theoretical models that describe the electro-disintegration of the deuteron such as Hummel and Tjon's relativistic model based on the one-boson-exchange model and relativistic Bethe-Salpeter equation [HumT89] and the model of Mosconi and Ricci [Mosc90] based on standard non-relativistic nuclear theory which includes relativistic corrections and MEC effects. One well respected model, developed in the late seventies is that of Fabian and Arenhövel [Fabi79].

Arenhövel's theoretical calculations [Aren88] [Aren92] [Aren99] [Aren00], which are non-relativistic in their approach, solve Schrödinger's equation using the Paris [Laco80] potential description for the nucleon-nucleon interaction to calculate the 2 nucleon bound and scattering states. The most important lowest-order effects included in the calculations are shown in figure 2.3

Arenhövel's theoretical calculation of P_0^y is shown in figure 2.4. Ideally one would like to take experimental measurements across the full θ range shown in the figure however the first goal of this commissioning experiment is to take a measurement of P_0^y at just one point at $\theta = 180°$ using HARP. A measurement at this point should be non-zero if we include FSI effects, so a measurement at this point with a 10% error would allow one to know if the theoretical model describes FSI correctly.

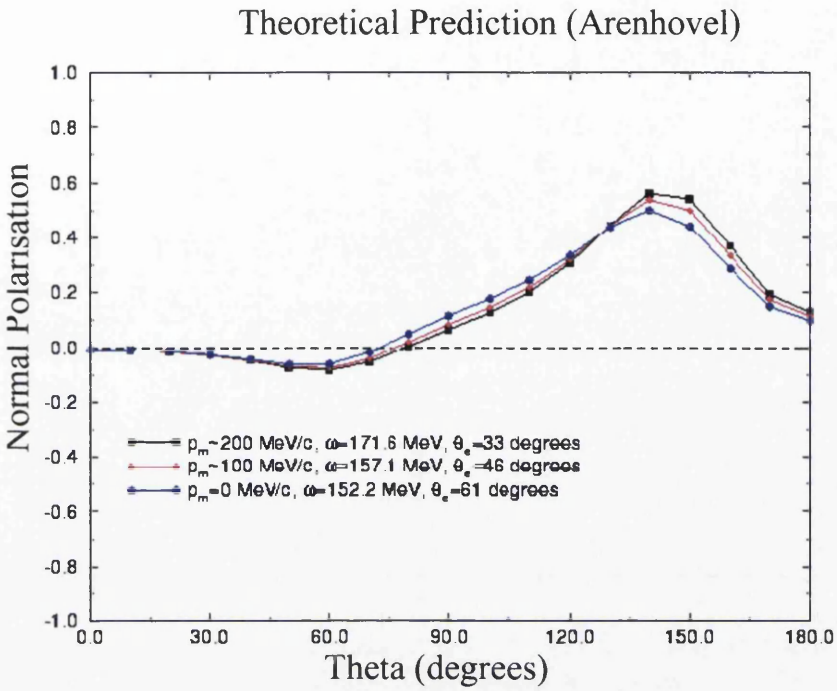

Figure 2.4: *Theoretical plot for P_0^y as a function of θ_{np} in centre-of-mass frame. The chosen experimental measurement point at $\theta = 180°$ shows the theoretical value of $P_0^y = 0.1$ expected.*

2.3 Electron accelerators

To probe distances of the order of nucleon diameters, we require incident electron energies in the order of 500 MeV. Since the electromagnetic force is relatively weak and the cross-section of electron-scattering reactions small in comparison to purely hadronic reactions, high beam intensities as well as greater thickness of targets are required to increase the rate of interactions.

The first electron accelerators used the synchrotron method to accelerate

electrons up to a few GeV. However, these electron beams had poor duty factor, typically less than 1%. Linear accelerators (linacs) improved upon this poor duty factor but with an adverse effect on the beam energy.

The basic linac can be described as a series of radio-frequency cavities which accelerate the electron beam in a straight line. Because resistive losses are high, the travelling electron wave is maintained by supplying power at regular intervals along the linac. Linacs can be operated in pulsed mode which reduces the amount of heat needed to be dissipated, but delivers a low duty factor electron beam.

With the advent of pulse stretcher rings which extract low duty factor beams from synchrotron or linear accelerators and of racetrack microtrons, very stable beams with 100% duty factor can be obtained.

In Mainz, the 850MeV Mainzer Microtron (MAMI) uses a racetrack configuration to obtain continuous wave (CW) electron beams. The electron beam is circulated around three microtron stages and at each stage accelerated in a short straight section. At the end of the third stage, an electron beam can be extracted and delivered into one of several experimental halls. In 1990, a CW 12μA beam with 100% duty factor was extracted from MAMI [Herm90].

In 1992, the 500 MeV, 1% duty factor linac (MEA) at NIKHEF was upgraded with the addition of the Amsterdam Pulse Stretcher (AmPS) ring [Witt93]. This made available a near-continuous wave electron beam with duty factor of $\approx$50% and beam current of 10μA. The AmPS facility is discussed further

in section 5.1.

With these improved accelerator facilities it is now possible for the first time to perform an experiment such as ^{2}H$(e, e'\vec{n})$ to measure the asymmetry.

2.4 Neutron detection

The neutron was discovered by Chadwick in 1932 [Chad32]. It was the first electrically neutral hadron to be discovered yet its detection still presents a challenge. Most particle detection techniques utilise the ionisation properties of the particle as it passes through matter. The neutron, however, does not produce ionisation directly when interacting with material and so neutron detectors must be based on detecting the secondary events produced by a nuclear reaction such as (n,p), (n,α), (n,γ) and so on. There are various methods which have been employed to detect the presence of the neutron. Two of the main methods, both of which can be expanded to measure P_0^y , are outlined below.

2.4.1 The time-of-flight method

The time-of-flight (TOF) determination (illustrated in figure 2.5) is probably the best known method for detecting neutrons.

The detection of the neutron is achieved using scintillators. The neutron produces a recoil proton in a secondary hadronic reaction which is then observed. The pulse height in the detector from this recoil proton is not proportional to the incoming neutron energy and therefore the neutron energy

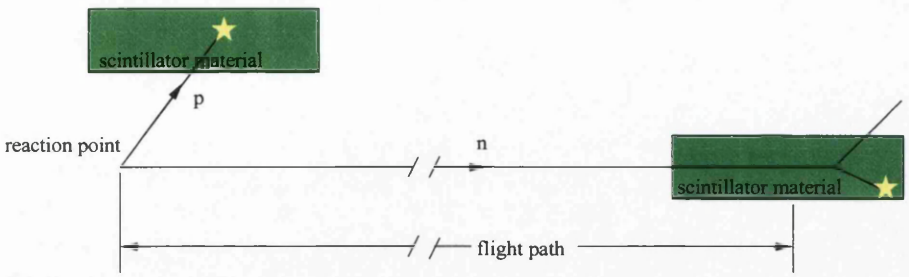

Figure 2.5: *The time-of-flight (TOF) method for determining neutron energies. The neutron flight pathlength is taken from the reaction point to the centre of the detecting plastic scintillator material.*

is determined from its flight time and the length of the flight path. However, as the neutron energy increases, the time-of-flight and hence energy resolution decreases. To compensate for this, the length of the flight path must be increased which then means a drop-off in the detection solid-angle. The neutron detection efficiency of the TOF method is dependent on the thickness of the scintillator detector. By increasing this thickness, the neutron reaction probability is increased but at the expense of energy resolution.

The measurement of polarisation variables using the time-of-flight set-up, as with the recoil proton detection (RPD) method, requires a secondary scattering process as illustrated in figure 2.6. Plastic scintillator material is used as an analyser where the secondary scattering process occurs providing the timing information. If the incoming neutron beam is polarised then the scattered neutrons exhibit an asymmetric angular distribution. These

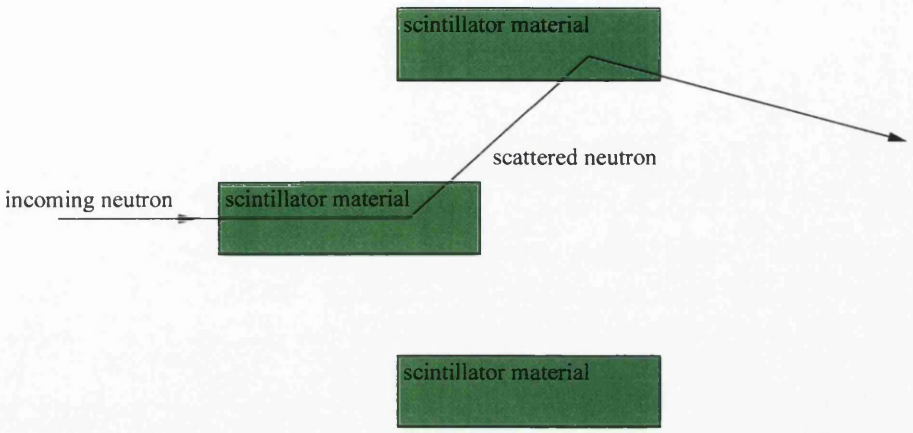

Figure 2.6: *The time-of-flight polarimeter set-up. The analyser consists of scintillator material in which the incoming neutron scatters. If the neutron beam is polarised, then the scattered neutrons exhibit an asymmetry. The scattered neutron is detected in scintillator banks on either side of the analyser with the normal TOF technique.*

scattered neutrons then need to be detected to determine any polarisation properties.

2.4.2 The recoil proton detection method

With the recoil proton detection (RPD) method, as with the TOF method, the nucleon polarisation and energy is determined through a secondary scattering reaction. The principle of the method is illustrated in figure 2.7; the incoming neutron undergoes a secondary scattering process in an analysing medium, knocking out a charged (recoil) particle.

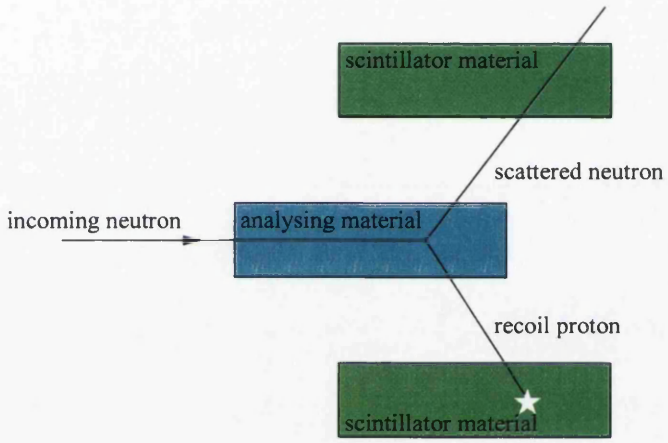

Figure 2.7: *The RPD technique. The incoming neutron is scattered elastically in an analysing medium, knocking out a proton. This recoil proton is then detected in a plastic scintillator detector and its energy determined. Using the knowledge of the scattering process and the proton's energy and angle, the energy of the incoming neutron can be determined.*

Detection of this recoil particle using conventional ionisation-technique detectors yields information on the neutron without explicit need to detect the neutron twice. Liquid hydrogen (LH_2) is used as the analyser since the (n,p) scattering process is the only possible final state (in contrast to that of all other nuclei which lead to a multitude of possible final states) and the cross-section and analysing powers (see figure 2.8) are well-known [Arnd81].

2.4.3 Measuring neutron polarisation with a polarimeter

A polarimeter makes use of the recoil proton detection technique to measure the polarisation of an incoming nucleon. This process is illustrated in figure 2.7. A secondary scattering or "analysing" medium is used in which the incoming neutron undergoes an elastic scattering mechanism. The left-right asymmetry of this secondary reaction leads to a measurement of the nucleon polarisation if the analysing power of the scattering medium is well known. The distribution of the recoil particles exhibits a left-right asymmetry due to the non-zero polarisation of the neutrons. This polarisation of the neutron determines the direction of the recoiling proton from the analysing medium: the difference between the number of recoil protons that are detected on either side of the analysing medium allows us to determine the average polarisation of the incoming neutrons. This can be described by:

$$P_n = \frac{1}{A_y(\theta_n, T_n)} \frac{N_\uparrow - N_\downarrow}{N_\uparrow + N_\downarrow} \tag{2.23}$$

where $N_\uparrow, N_\downarrow$ represent the number of recoil protons detected on either

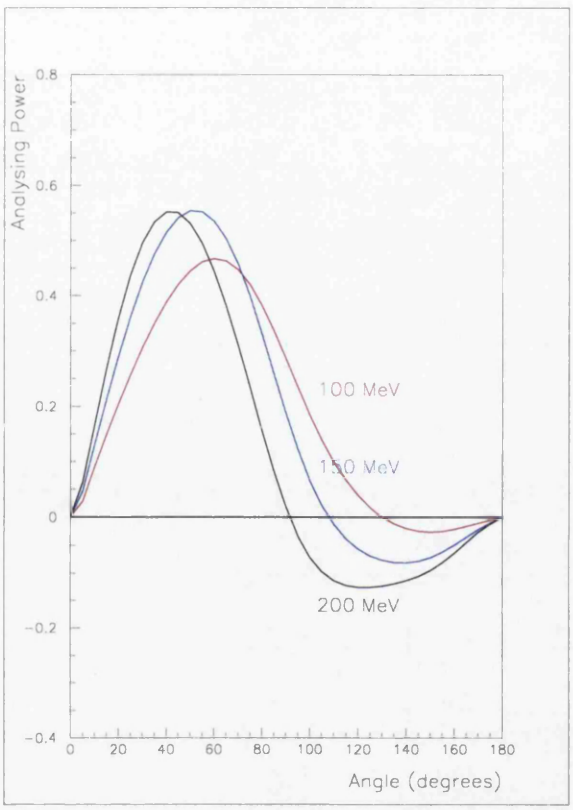

Figure 2.8: *The analysing power of hydrogen for for n-p scattering for a range of incoming neutron energies. The angle given is for the centre-of-mass frame.*

side of the vessel. A_y is the analysing power of the (n,p) reaction and is defined as:

$$A_y(\theta_n, T_n) = \frac{\sigma_+(\theta_n) \; - \; \sigma_-(\theta_n)}{\sigma_+(\theta_n) \; + \; \sigma_-(\theta_n)} \tag{2.24}$$

with $\sigma_{+/-}(\theta_n)$ defined as the differential (n,p) cross-sections for anti-parallel($\sigma_-(\theta_n)$) and parallel($\sigma_+(\theta_n)$) components of spin with respect to the secondary scattering plane. It should be noted that A_y is dependent on θ_n, the polar scattering angle of the ejected neutron, as well as incident neutron energy T_n and so can change sign in n-p scattering (see figure 2.8). One should therefore avoid integrating over the entire range of θ_n, but rather take measurements across a range of θ_n that will not lead to a loss of information in A_y.

The high acceptance recoil polarimeter is a new polarimeter which employed this technique and was used in the ^{2}H$(e, e'\vec{n})$ experiment at NIKHEF. The detector is discussed further in chapter 3.

Chapter 3

The High Acceptance Recoil Polarimeter (HARP)

The High Acceptance Recoil Polarimeter (HARP) is a new detector system based on the recoil proton detection (RPD) technique which has been designed to measure the energy and polarisation of incoming nucleons. HARP was commissioned early in 1997 and its involvement in the $^2\mathrm{H}(e, e'\vec{n})$ experiment was its first real physics experiment. An overview of the detector is given in section 3.1 and each of the main detector elements are then discussed in the following sections.

3.1 Overview of the detector

To measure the polarisation, HARP needs to measure asymmetries and so the detector geometry is symmetrically designed. An overview of the HARP design is given in figure 3.1. At the heart of the detector is a liquid hydrogen (LH_2) vessel which acts as a secondary scattering target and analysing medium for incoming nucleons. These incoming nucleons undergo an elastic (n, p) reaction (thus giving the vessel the alternative name of 'converter') with the recoiling proton detected to obtain information about the initial properties of the incoming nucleon.

In front of the converter is a charged particle tagger. This consists of thin scintillator strips which can detect the passage of charged particles. It therefore becomes possible to distinguish between incoming charged and uncharged particles.

Symmetrically positioned wire chambers are placed on either side of the

converter to detect the charged particles passing through and enabling the reconstruction of the tracks. This spatial information is used to determine the precise kinematics of the secondary scattering process. As is revealed in champer 6, the wire chamber information was not available in the final experiment which had an impact on the resolution of the spatial information used in the analysis. Finally, two arrays of plastic scintillators are positioned at the outer edges of the HARP box. The recoiling particles are stopped in these scintillator arrays and the energy they deposit is measured. From this information and the scattering angle deduced from the wire chamber information, it is possible to obtain the initial kinetic energy and polarisation of the incident nucleon.

All detector elements are held in a steel cradle which allows the possibility of rotating the detector around its centre (so that the scintillator telescope banks can be positioned either above and below or to the left and right of the liquid H_2). An area between HARP and the primary target is left for a lead collimator and the entire detector can be further surrounded by concrete to provide shielding against background. Hence only the converter and particle tagger are exposed to the incoming reaction flux with the rest of the detector elements shielded from the very bright source of noise that the primary target represents.

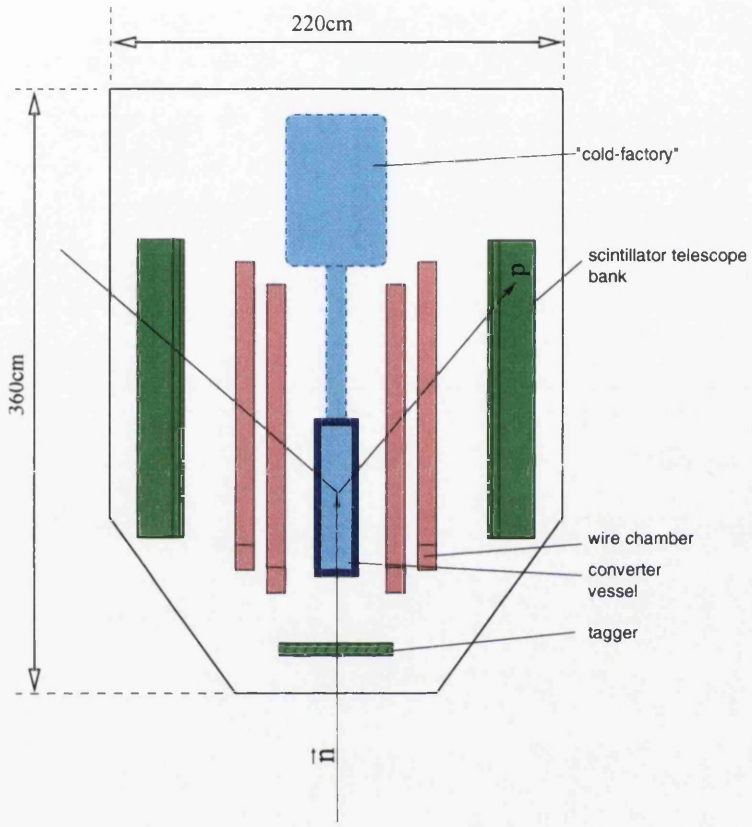

Figure 3.1: *A schematic view of the HARP detector. This top-down view shows the tagger at the front of the detector with the converter directly behind. On either side of the converter are the wire chambers and scintillators. The "cold-factory" is shown at the rear of the HARP box.*

3.1.1 The liquid hydrogen converter

The cryogenic converter is the heart of the HARP detector [Uden97]. It was designed and constructed at NIKHEF and consists of two main elements: the LH_2 volume where the secondary elastic reaction occurs, and the cryogenic unit (or "cold-factory") which liquifies the hydrogen from a gaseous source. The LH_2 volume (illustrated in figure 3.2) consists of two rectangular windows each with dimensions $2 \times 10 \times 60$cm contained in a steel frame with dimensions $5 \times 25 \times 65$cm. The LH_2 vessel is flat and rectangular rather than the conventional cylindrical shape: this minimises background noise from the metal frame, as well as increasing energy resolution by decreasing the uncertainty of the secondary reaction interaction point. This also allows the wire-chambers to be positioned closer to the secondary reaction vertex, thus increasing the angular resolution of the chambers when determining the track of the knocked out proton.

The "cold-factory" uses two separate cooling systems: a hydrogen system and a helium system.

A minicooler (type Leybold RW580) is used to liquify the hydrogen gas into the 4.5 litres of LH_2 required inside the vessel. This cooling process is performed in 2 stages: the first cools the hydrogen to 80K and the second stage brings the temperature down to 20K. The total time required to condense all the hydrogen is approximately 22 hours. The liquid hydrogen flows to the reaction volume under the force of gravity and, once full, begins flowing into a buffer vessel above the converter. In this way, the liquid-vapour

interface is kept outside the reaction volume and the formation of gas bubbles within the converter vessel is prevented.

A heater in the vessel ensures that the LH_2 within the buffer is kept at a slightly higher temperature ($\approx$1K) than that of the LH_2 in the converter; sensors in the buffer vessel allow measurement of the level of liquid hydrogen so that the adjustments to the temperature can be made accurately.

Very good heat insulation is required but insulation material has to be kept to a minimum to avoid energy loss and restriction of low-energy protons "converted" in the vessel.

To minimise requirements for insulation, a second cooling system is used to pump liquid helium around the converter system. This acts as a heat sink, helping to maintain the temperature of the liquid hydrogen without the need for bulky insulation material. The helium system employs a RW1245 minicooler to cool the helium gas down to 20K.

The cryogenic system is monitored and controlled using a series of 12 commercially available heat sensors placed around the cryogenic system. A LakeShore temperature controller (LakeShore Cryoronics Inc., Model DR-C93) and a Programmable Logic Controller (a small computer which performs simple logic on input signals and produces output signals on the basis of programmed instructions) are used to ensure the safe operation of the system.

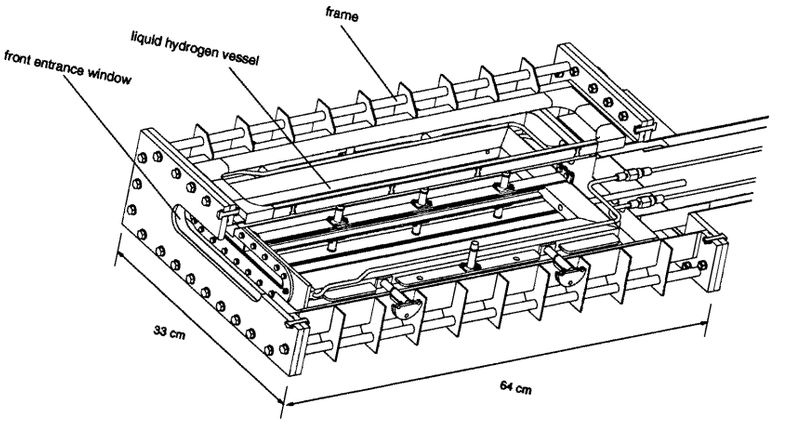

Figure 3.2: *Cut-away view of the liquid hydrogen vessel where the secondary scattering process occurs.*

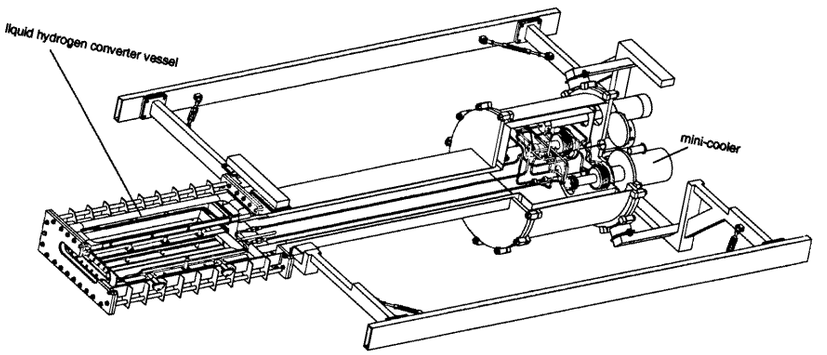

Figure 3.3: *Overview of the liquid hydrogen system in its frame. The vessel can be seen at the front the 'cold factory' positioned at the rear.*

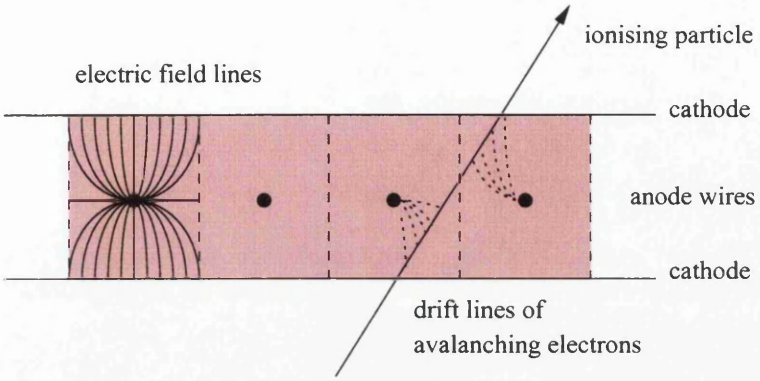

Figure 3.4: *Cross section through a MWPC. The electric field lines inside the chamber are illustrated to the left. To the right, the drift lines of free electrons caused by the traversing charged particle are shown.*

3.1.2 The wire-chambers

In order to track the recoiling protons from the secondary reaction, multi-wire proportional chambers (MWPCs) are used.

MWPCs consist of an array of thin wires inside a chamber filled with a gaseous medium. A high voltage is applied across the wires creating electric field lines as illustrated in figure 3.4. A charged particle crossing through the chamber will ionise the atoms/molecules of the gas, thus creating free electrons and charged ions. The number of these primary electron-ion pairs is proportional to the energy of the ionising particle entering the chamber.

The electric field within the chamber causes the free electrons/ions to accelerate in opposite directions along the field lines. The free electrons will

collide with the gas molecules and in turn, if they have sufficient energy, create secondary electron-ion pairs. These secondary particles undergo the same process of being accelerated along the field lines and further ionising the chamber gas. This electron "avalanche" can then be detected allowing the passage of the ionising particle to be observed. The voltage applied to the wires of a MWPC must be high enough to give the transversing particle to be detected sufficient energy to cause an "avalanche" without breaking down the gas inside the chamber, thus causing sparking and damaging the wires. The gas inside the chamber must be chosen to allow the avalance process, but limit the mean free path of collisions in order to avoid too much current passing through the chambers. The gas must also be constantly renewed to replace the molecules stripped of electrons and keep the overall ionisation efficiency high.

HARP can accomodate a total of six such chambers (three symmetrically positioned on either side of the LH_2 vessel) although only a total of four were actually available during the $^2H(e, e'\vec{n})$ experiment.

The wire chambers were designed at ISN-Grenoble and constructed at the NIKHEF workshops. Each of the chambers consists of two planes of 448 thin anode wires spaced 3mm apart, each sandwiched between two cathode foils. Two planes of these wires are present in each chamber, one rotated 90° with respect to the other enabling spatial information in the x and z planes to be recorded. The cathode foils are separated 6mm by a Stesalit [1] frame.

[1]Stesalit is an insulated epoxy compound material which is used in wire chamber construction because of its good insulating and mechanical properties.

No. active wires	448
No. guard wires	8
wire material	gold plated 95% tungsten 5% rhenium
tension	0.72 Nm^{-1}
wire diameter	25μm
span length	1668 mm

Table 3.1: *HARP MWPC wire characteristics*

Two additional foils, 25μm thin aluminium coated mylar, are used for the outside windows. These are used because of a slight overpressure inside the chamber due to the ionising gas present which causes a bulging of the outside foils. If the cathode foils were the barrier between the chamber gas and the outside air, the uniform electric field within the chamber would be lost. Using these additional foils for outside windows has some added advantages: oxygen molecules which diffuse through the foil are kept outside the active volume and, because the foils are grounded, they also shield against high frequency noise.

A mixture of 90% Argon and 10% Methane is used as the ionising medium inside the chambers. This mixture is passed as a continuous flow around each chamber.

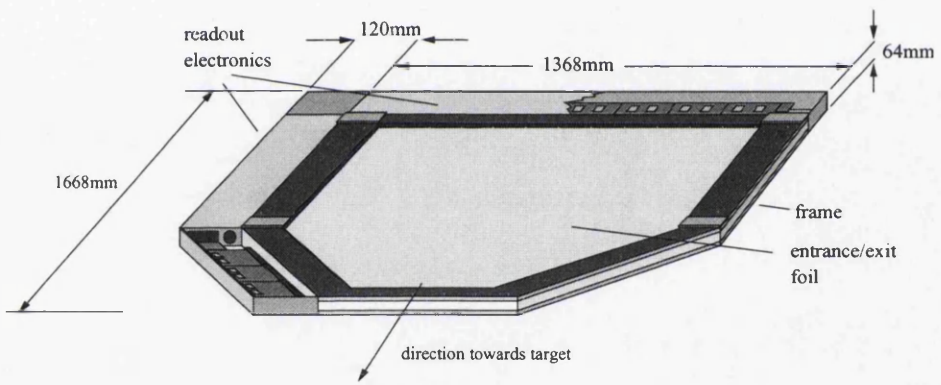

Figure 3.5: *An exploded view of a wire chamber showing the positioning of the readout electronics around two edges of the frame.*

3.1.3 Scintillator telescopes

An array of 4 scintillator telescopes are positioned symmetrically on either side of the LH_2 converter vessel. These telescopes each consist of 3 plastic scintillator bars: 2 thin ΔE strips and a thick stopping E bar. Each telescope is of identical design as illustrated in figure 3.6. To position the telescopes as close to the front of HARP as possible, each incorporates a curved light guide at the front. Charged particles interacting with the scintillator material cause excitation and subsequent emission of photons. These photons travel along the length of the scintillator bar and are measured using photo-multiplier tubes (type Burle 8575 and Burle 8854) which are positioned at each end. The signal produced can then be used to determine the energy of the charged particle and its interaction point along the bar (see chapter 6).

The front and second ΔE strip are 3mm and 10mm thick respectively with the stopping E bar, 200mm thick (figure 3.7). The scintillator bars are labelled from front to rear as D, M and E [2]. This arrangement enables recoil protons to be detected and identified for a wide range of energies: the 3mm and 10mm strips are used to stop and identify low energy protons (20-60MeV) and for higher energy protons, the thicker E bar is used in conjunction with one of the ΔE bars (see figure 3.7).

A PMT front-end board for each telescope processes the signals from the 3 pairs of PMTs. A coincidence between a pair of PMTs at each end of

[2]The D and M scintillator labels are taken from the first letter of the dutch words *dun* and *middle* which translate as *thin* and *medium* respectively.

a scintillator bar is mandatory for a valid event and this defines a zero-level trigger condition for HARP. By establishing a coincidence between the thick E and one of the thinner scintillator bars, and by reducing the coincidence time window between these events, one can quickly determine the validity of an event detected in the telescope. This is discussed further in section 3.2.

A photo multiplier tube (PMT) front-end board for each telescope processes the signals from the 3 pairs of PMTs. A coincidence between PMTs at each end of a scintillator bar is required for a valid event and this is one of the zero-level trigger events of the HARP detector. One can then quickly determine the validity of an event caused by a particle passing through the scintillator telescope by establishing a coincidence, within a suitable narrow time window, between the E bar and one of the thinner bars.

The telescopes are constructed using BC400 plastic material (Bicron Corporation) and are 160cm in length with a spatial resolution calculated to be 8cm. The response of these scintillator telescopes has been previously documented in full [Boer95].

The information obtained by the telescopes can then be used in conjunction with the wire chamber information to obtain the energy and scattering angle of the recoil proton and hence determine the energy of the incoming nucleon.

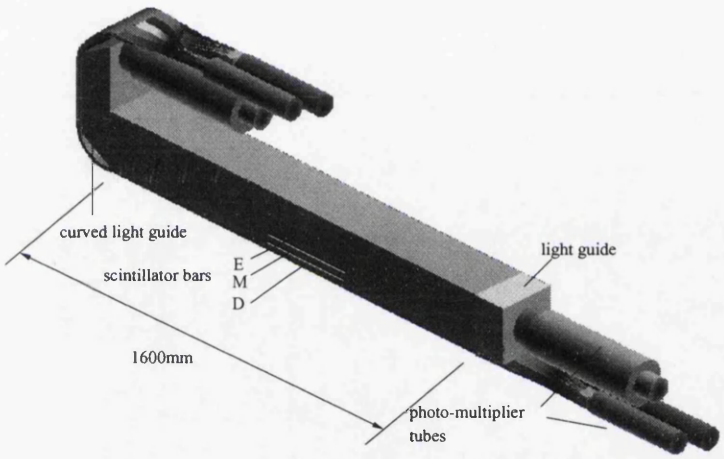

Figure 3.6: *View of a single scintillator telescope incorporating the D, M and E bars. The light-guides are shown: the curved light-guides are at the front of the bar with the straight guides to the rear.*

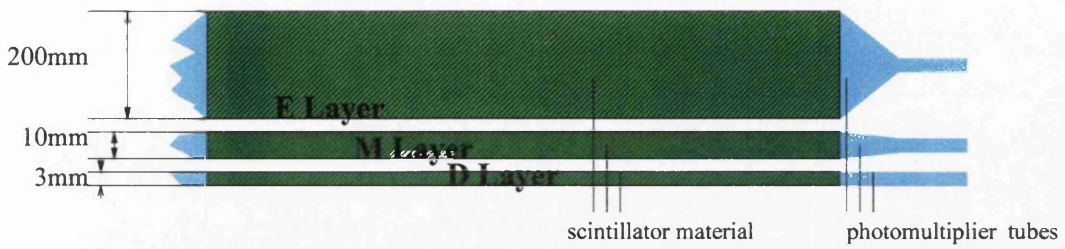

Figure 3.7: *Schematic diagram of the 3 layers in each of the scintillator telescopes. The layers are named E, M and D according to their thickness, with E the thickest and furthest away from the converter vessel when installed in the HARP frame and D the thinnest and closest.*

3.1.4 Charged particle tagger

Mounted at the front of HARP is an array of 15 thin scintillator strips which act as a tagging device to distinguish between charged and neutral incoming particles. The scintillator strips are 30mm wide and 53mm in length and are interleaved in two overlapping rows (illustrated in figure 3.8) of 7 and 8 strips. The double overlapping layers were incorporated to allow coincidence checks and therefore achieve good background discrimination. The front layer strips are 1.6mm thick while the rear layer strips are 3.2mm thick. Each strip is wrapped in aluminized mylar to reduce loss of reflected light within. Each strip is constructed from the same BC400 material used for the scintillator telescopes outlined in section 3.1.3 and is individually read out with a small photomultiplier tube (type Phillips XP 1991).

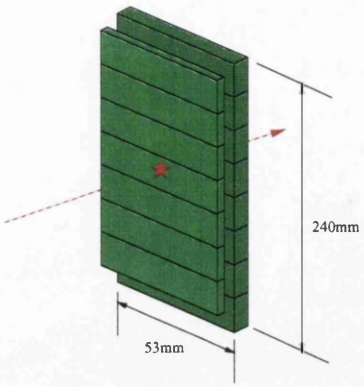

Figure 3.8: *Layout of the charged particle tagger. A rear layer of 8, 3mm thick scintillator strips is overlaid by a front layer of 7, 1.6mm thick scintillator strips. A charged particle passing through the tagger will be detected in each layer enabling a selection process to be made. The two-layer design allows background noise to be cut.*

The detection probability of charged particles has been measured and a detection efficiency for the tagger array has been determined at 99.9% [Munz96]. This is then a useful tagger, enabling the identification of proton events which would undergo $(p, 2p)$ scattering within HARP.

3.2 The HARP trigger

HARP has several trigger levels which must be satisfied before an event is deemed relevant. The zero-level trigger relates to the photomultiplier tube front-end electronics and has been mentioned briefly in section 3.1.3. This trigger determines that a valid event has occurred within a scintillator tele-

scope by checking for a valid hit in the M bar, in coincidence with a hit in either the D or E bars. A schematic diagram of the HARP trigger electronics is given in figure 3.9.

The definition of a valid hit is determined by the coincidence of front and rear PMT signals from a scintillator bar. This is done using a device known as the mean-timer which is employed to overcome the long coincidence time windows caused by the long scintillator bars.

The mean-timer circuit (illustrated in figure 3.10) ensures that a coincidence is measured even if the individual pulses are shorter than the spread of their relative timing. The time resolution of the mean-timer is set by the spacing of the ECL gates which, as shown in figure 3.10, is 1.5ns.

Each zero level trigger is then fed to trigger level one which consists of an OR of all telescope triggers. This level one trigger is then passed on to the Master Coincidence Unit (MCU) which is external to HARP. The MCU collects triggers from all detector arms involved in the experiment, in this case from the quadrupole-dipole-quadrupole (QDQ) spectrometer and issues an Event Trigger (ETR) should a coincidence between HARP and the QDQ be detected.

This ETR is sent back to HARP whereupon the extensive HARP event information (consisting of all QDC and TDC readouts for each PMT and tagger strip as well as all wire chamber information) can be read. Should the ETR not arrive within a specific time window, the HARP electronics are cleared ready for the next event.

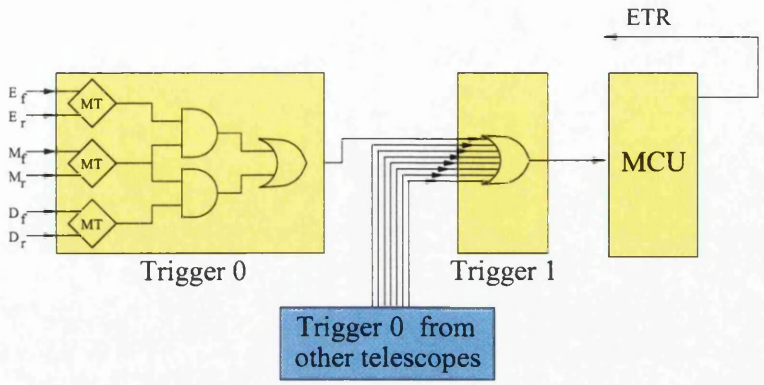

Figure 3.9: *Schematic representation of the HARP trigger logic. The signals from the front and rear scintillator strip PMTs are fed into a mean-timer (denoted by 'MT'). The final coincidence is output to the Master Coincidence Unit (MCU) which then sends an ETR signal to the overall data acquisition system for an experiment.*

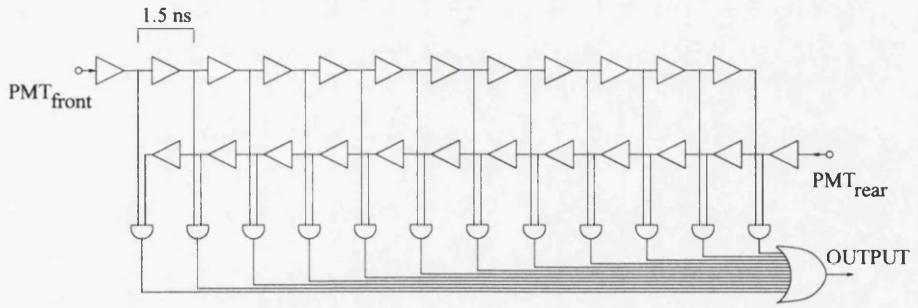

Figure 3.10: *The mean-timer circuit. The coincidence between pulses from the front and rear PMTs of a scintillator bar in a telescope are determined through the array of digital delay and AND gate modules. The result from all the coincidence gates are submitted to a twelve-fold OR gate.*

3.3 The gas safety system

Using relatively large amounts of liquid hydrogen in an electron-scattering environment raises concerns for safety; the explosive nature of hydrogen (mixed with oxygen) and the possibility of "sparking" inside the HARP box from the high-voltage read-out electronics could have a devastating effect.

In order to reduce this risk, the HARP box is filled with nitrogen to prevent the creation of the explosive hydrogen-oxygen mixture should an unwanted escape of hydrogen be released into the system. The HARP box is not completely air-tight and so a continual flow of nitrogen is required to ensure that the level of oxygen inside HARP is kept below a critical 5% limit.

As an additional safety feature, a *polyflow* exhaust connects the hydrogen system directly to outside the experimental hall should an emergency evacuation of the hydrogen be required.

The safety system is monitored at all times using an application of *LabWindows* [Nic93] which provides a report of all systems and warns of any breaches of system pre-set limits.

3.4 Phases of construction

It was decided to build HARP in two phases. The first phase of construction involved a fully functioning detector system. Plans for the second phase were to increase the amount of converting LH_2 by enlarging the converter vessel from the flat-rectangular shape to something more flat-trapezoidal measuring

	Phase I	Phase II
Converter Volume	2250cm^3	9750cm^3
No. Telescope	8	16
No. Wirechambers	4	6
No. Tagger Strips	15	34
PMTs	63	130

Table 3.2: *Overview of the construction differences between the first and second phase of HARP.*

50*cm* wide at the front and 80*cm* at the rear. In addition, the Phase II design included doubling the number of scintillator telescopes, increasing the number of scintillator strips in the charged particle tagger and adding a third wire-chamber to each side of the detector. Table 3.2 gives an overview of the differences between the two phases of HARP's construction.

Chapter 4

Commissioning Experiment

In November 1996 the cryogenic vessel, wire-chambers and scintillator arrays were assembled for the first time with the data acquisition system up and running.

In order to test HARP and the data acquisition system, the detector was involved in a commissioning experiment. This experiment was carried out in the EMIN hall at NIKHEF where an electron beam impinged on a liquid deuterium target. A beam current of $\approx 2\mu$A and energy of 591.5 MeV was maintained with a duty factor of 50% for the experiment. HARP was positioned at 45° with respect to the beam line with the QDQ spectrometer used to detect the coincident electrons. The EMIN hall, QDQ spectrometer and the pulse strecher ring used to provide the electron beam are discussed in more detail in chapter 5.

In section 4.1 a brief overview of the data acquisition system testing and the data taken during this experiment is given. Section 4.2 is devoted to the testing and analysis of the wire chambers which was carried out using the data obtained from the commissioning experiment. Finally a discussion of the analysis of the cryogenic converter and the scintillator telescopes is presented in section 4.3 along with a conclusion to the commissioning experiment results.

4.1 Data acquisition

The data acquisition hardware developed for HARP was based around a VME (IEEE1014-1987) crate which housed a central processing unit (CPU) and a control module named "module maître" (see figure 4.1). The CPU runs a real-time UNIX-based operating system, *VxWorks*, on which the data acquisition software is run. The module maître is responsible for the read-out of the front-end electronics (specifically the 16-bit analogue to digital converters, ADC16, of the photomultipliers and the custom built 32-bit chips, CPT32 [1] , designed for processing the information from the wire-chambers). This data is read across the ABUS, a proprietory token-ring data bus, and stored in a First In First Out (FIFO) buffer where it can be transported over an ethernet network to a host workstation. The data can then be analysed online or stored on magnetic media.

4.1.1 Data acquisition software

HARP is a new detector system and its data acquisition system required bespoke software to be developed to read and process the measured data. This software was developed over a two month period using a mock set-up of the detector and custom-built hardware to simulate event data. The speed of the software was vital in order to minimise deadtime and so was written in 'C' and compiled to run on a real-time operating system, *VxWorks* (a

[1] "ComPTeurs 32" - application-specific integrated circuits developed by the "CAO Electronique" group at ISN Grenoble

cut-down UNIX operating system designed specifically for real-time tasks).

Once complete, the data acquisition systems and its software were shipped to NIKHEF where they were integrated with the institutes existing data acquisition electronics. Various incompatibilities with data transport protocols were resolved and the software was shown to perform to the standard required under experiment conditions.

4.2 Evaluation of the HARP wire-chambers

The manufacture of the first HARP wire-chamber was completed in late 1995. Once it had been tested for mechanical stability and gas tightness, it was ready to undergo various tests to measure its detection efficiency under laboratory conditions. These tests performed in early 1996 used an electron source, ^{90}Sr, to provide ionising particles and two paddle scintillators as illustrated in figure 4.2. A scintillator was placed above and below the wire-chamber: a thin 1/2mm scintillator above and a thicker, 10mm scintillator below.

Using this arrangement, it was possible to measure the detection efficiency of the chamber under various conditions. Results of the first laboratory measurements are given in table 4.1 [Grun96].

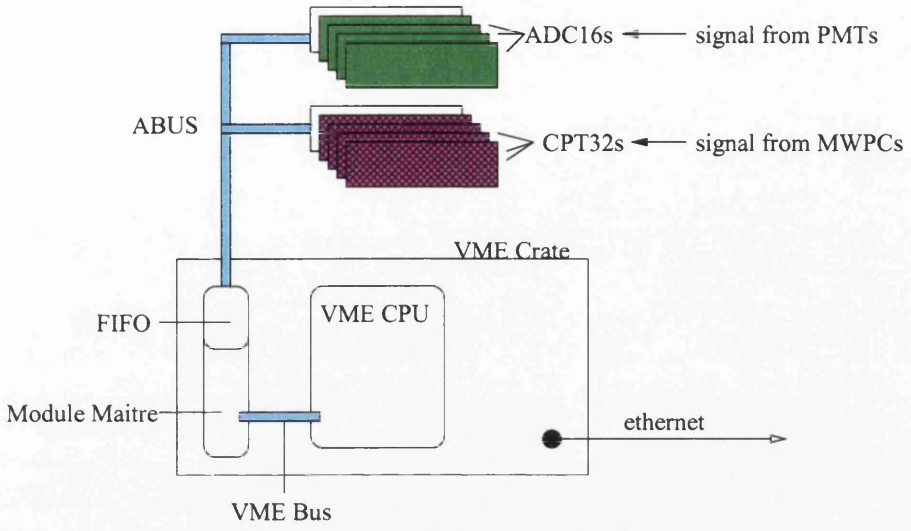

Figure 4.1: *The data acquisition set-up for HARP incorporating the VME crate and CPU with the module maître.*

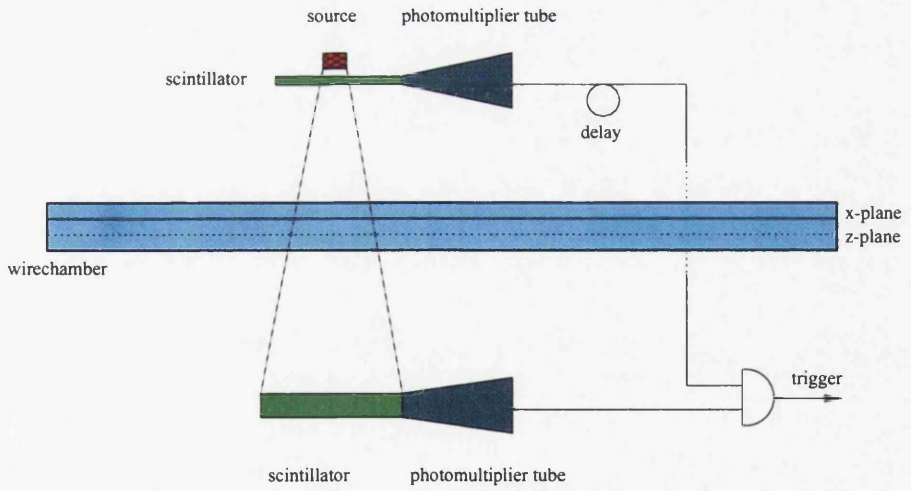

Figure 4.2: *Testing the efficiency of the wire-chambers in laboratory conditions.*

Voltage (V)	Efficiency (x-plane)	Efficiency (z-plane)
2420	50%	55%
2460	80%	86%
2480	94%	96%
2500	99%	99%

Table 4.1: *HARP MWPC efficiency measurements per plane in laboratory conditions. Chamber three was used for the purpose of the measurements.*

4.2.1 Further testing of the wire-chambers

The data from the commissioning experiment was collected and analysed: data analysis software was written to extract meaningful information from the raw data obtained. This software needed to manipulate the data and perform various calculations before exporting the data in a format that could be analysed by a more complex analysis package.

The first round of analysis revealed a number of "hot" wires: wires within the chamber that were over-sensitive to background noise and which triggered continuously (see figure 4.3).

An attempt to compensate for these "hot-wires" was made in the analysis software by allowing the software to make intelligent decisions about a hot wire's contribution to a valid event. With this method to veto obviously spurious information, the detection efficiency for each plane could be calculated. The rather disappointing results for chambers 1 and 2 are given in

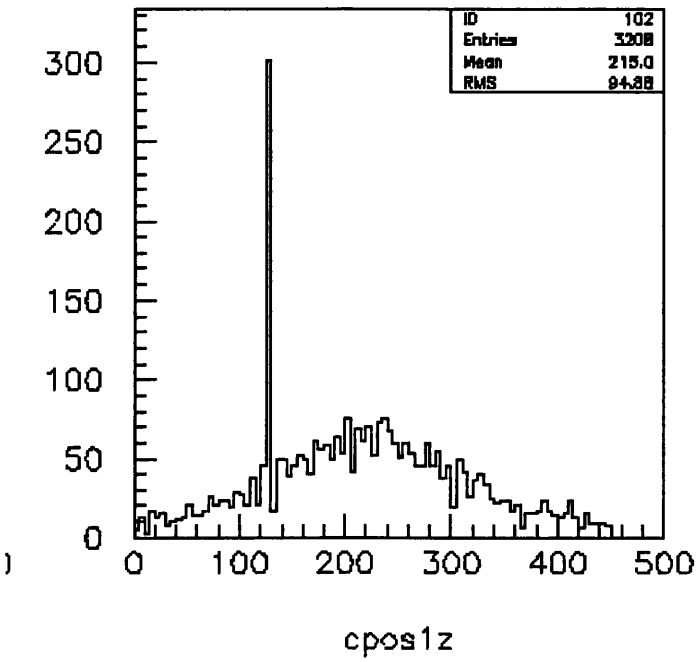

Figure 4.3: *Illustration of the problem with 'hot-wires'. A 'hot-wire' is a wire in the chamber which is over-sensitive to background noise giving a 'hit' for every event and distorting the true spectra. Highlighted above is wire number 128 in the Z plane of chamber 1. To overcome this problem it is necessary to eliminate these problem wires using software cuts.*

table 4.2. Only chambers 1 and 2 were analysed from the commissioning data. This was due to the fact that during the commissioning experiment, chamber 3 had become unoperational because of broken wires and so made efficiency calculations on that side of the detector impossible. The broken wires in chamber 3 were caused by "sparking" between the chambers wires and the cathode.

Although the detection efficiency of the wire-chambers was poor, it was still possible to reconstruct the tracks of protons knocked out of the converter vessel in the secondary scattering reaction. By taking the hit positions in two adjacent wire-chambers for a valid event, it is possible to reconstruct the scattered protons path and angle (see figure 4.4).

The analysis highlighted an obvious problem: the operating voltage of the chambers was too low. In addition it became apparent that thresholds on the read-out electronics were not sufficient to exclude the large amount of background noise.

The failure of chamber 3 and its implications added to the list of problems brought to light during the commissioning experiment: the chambers could not operate stabily at voltages much higher than 2500V, but efficiencies below this voltage were poor. All of these problems needed to be addressed so that HARP could reach its full potential. This is discussed in the following section.

	Voltage		
Plane	2300	2380	2530
wc1-x	5%	6%	7%
wc1-z	4%	5%	6%
wc2-x	4%	10%	22%
wc2-z	4%	10%	21%

Table 4.2: *Detection efficiency measurements from commissioning experiment. The low values were attributed to a combination of insufficient shielding around the detector system, low operating voltages of the chambers and low wire-chamber threshold settings.*

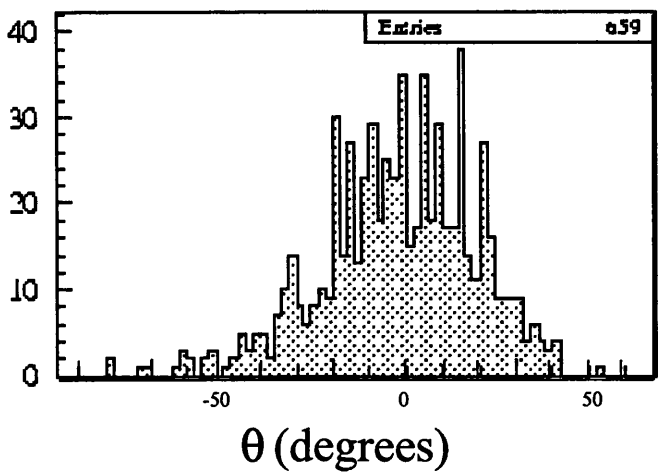

Figure 4.4: *The reconstruction of the secondary scattering angle within HARP using the information obtained from two adjacent wire-chambers.*

4.2.2 Re-evaluation of the wire-chambers

Following the analysis of the commissioning data, the wire-chambers were disassembled and the "hot-wires" highlighted in the analysis were replaced. In addition, a resistor-capacitor (RC) coupling was added between each wire and the read-out electronics in all four chambers to reduce the leakage current. It was envisioned that this would allow the chambers to operate stabily at higher voltages. With the alterations made, HARP was re-assembled at NIKHEF in July 1997 and the detection efficiency of each chamber re-evaluated using both cosmic and radioactive source in a manner similar to that illustrated in figure 4.2. Marked improvements over the efficiencies measured during the commissioning experiment were calculated as illustrated in table 4.3.

4.3 Conclusion

The data acquisition software operated smoothly during both mock set-up tests and the commissioning experiment: its stable running on the VME CPU integrated well with the NIKHEF data acquisition system and the HARP system performed well with other detectors of the experimental hall.

The analysis of the wire-chambers highlighted some problems with their construction: their operation in the high background environment of the commissioning experiment did not live up to the design expectations although an attempt to compensate this problem was made by making a minor mod-

	Voltage		
Plane	2300	2400	2510
wc1-x	25%	61%	89%
wc1-z	24%	69%	92%
wc2-x	30%	61%	89%
wc2-z	29%	68%	91%
wc3-x	22%	62%	84%
wc3-z	29%	70%	95%
wc4-x	23%	64%	89%
wc4-z	30%	70%	92%

Table 4.3: *Detection efficiency measurements for the wire-chambers after the removal of the problem 'hot wires'.*

ification to the design.

Detection efficiencies of ≈84-92% were measured for the wire-chambers during the final testing phases where HARP was fully assembled. This result was a great improvement on the values obtained during the commissioning experiment (table 4.2). The wire chambers provided a resolution of 2° in θ. The operational effect on the wire-chambers made by the RC coupling modification could not be determined in the final test and the full implications of this modification would have to wait until the full experiment detailed in the next chapter.

In addition to the results presented previously, analysis was also undertaken in parallel on the performance of the charged particle tagger, the cryogenic converter and the scintillator telescope arrays. The tagger was determined to reach a detection efficiency for charged particles of 99.9% during the commissioning experiment [Munz97]. The cryogenic converter operated stabily for the two weeks of the commissioning experiment [Uden97] and the scintillator telescopes were calibrated and a coincidence timing peak width of 3.3ns and a positional resolution of 8cm obtained [Schi97].

Chapter 5

The ^{2}H$(e, e'\vec{n})$ Experimental Set-up

This chapter describes the general experimental set-up used in the ^{2}H$(e, e'\vec{n})$ experiment. HARP has been described in detail in chapter 3 and so only the remaining experimental apparatus is described here. An overview of the general set-up is shown in figure 5.1.

The experiment was performed in the EMIN hall at the National Institute for Nuclear Physics and High Energy Physics (NIKHEF) using the extracted high-duty factor electron beam from the Amsterdam Pulse Stretcher (AmPS) [Witt93]. For the detection of the scattered electrons, a high resolution quadrupole-dipole-quadrupole (QDQ) spectrometer was used [Vrie90].

5.1 The electron accelerator facility

The electron accelerator facility at NIKHEF consists of a linear accelerator (the Medium Energy Accelerator, MEA) and a stretcher ring (the Amsterdam Pulse Stretcher, AmPS). An overview of the facility is illustrated in figure 5.2.

The linear accelerator (MEA) delivers a low duty cycle pulsed electron beam (0.7 μs or 2.1μs width corresponding to 1 or 3 turn injections) which is injected into the stretcher ring (AmPS) where it is stored. The beam is circulated around the ring and stretched until a high duty factor continuous-wave beam is produced.

This stretched beam is then slowly extracted over many turns and delivered to the scattering chamber in the EMIN hall. A current of 10μA is

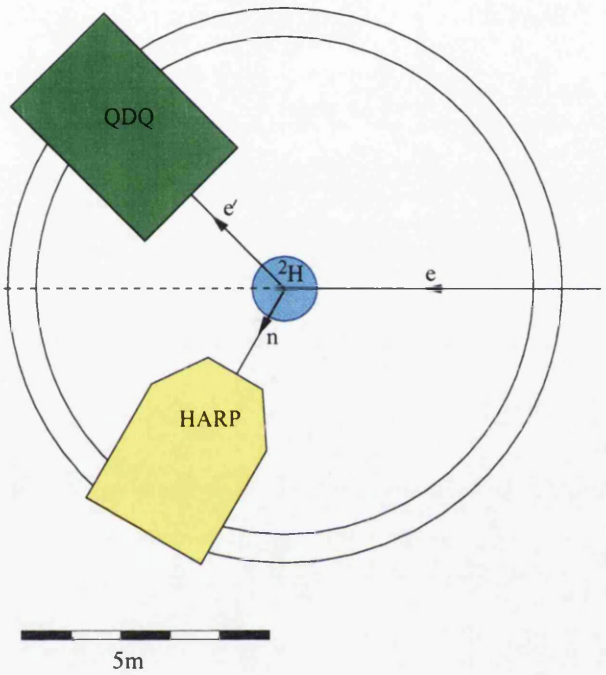

Figure 5.1: *Experimental layout in the Emin hall. Shown schematically are HARP and the QDQ spectrometer. At the centre is the liquid deuterium target. A rule is shown to give an idea of the scale of the detector layout, but it should be noted that the primary target cell (≈2cm in diameter) has been exaggerated for illustration purposes.*

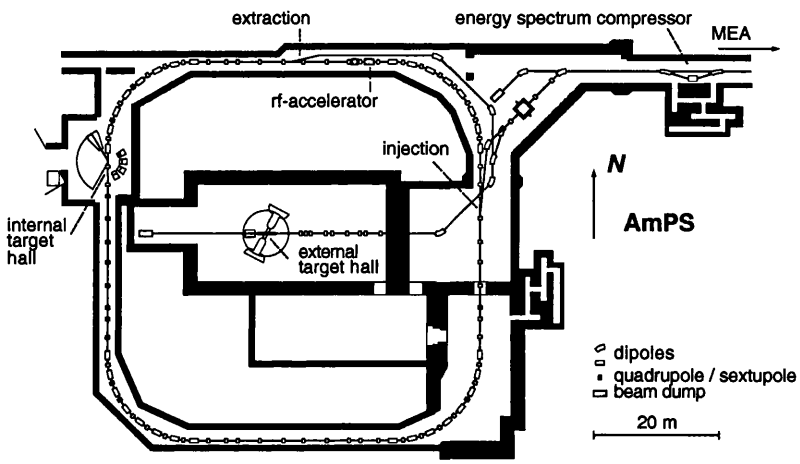

Figure 5.2: *Schematical view of the AmPS ring. From MEA at the right the electrons are injected. At the top a part of the beam is extracted and lead to the external target hall in the middle.*

possible for the 600MeV beam with a duty factor of 50%.

5.2 The QDQ spectrometer

The Quadrupole-Dipole-Quadrupole (QDQ) spectrometer was used to detect the scattered electrons. It is of conventional magnetic spectrometer design which uses a quadruple-dipole-quadruple magnet configuration to bend the trajectories of incoming charged particles. In the uniform magnetic field, the momentum of the particle defines the radius of curvature of its path. By measuring this radius and using the known mass, the momentum and hence energy of the incoming particle can be determined.

The spectrometer has an entrance quadrupole to limit the accepted trajectory dimension in the non-dispersive direction which increases the detector's resolving power. The magnets are forged from low-carbon steel with a flatness of the poles better than $\pm 3mm$ and a plan-parallelism of $\pm 6mm$ in order to achieve the field homogeneity required to obtain its high-resolution. Four multi-wire drift chambers (MWDCs) detect and track the path of the scattered electrons at the focal plane. The trigger detector for the spectrometer consists of a scintillator and Cherenkov counter. The aerogel Cherenkov radiator is used in pion production experiments where large electron suppression is required.

The layout of the QDQ is shown in figure 5.3 and 5.4. The QDQ spectrometer weighs 145 tonnes (including 94 tonnes of shielding) and is rotated

around the scattering chamber on roller-bearings and levelled into position using 2 hydraulic jacks. The shielding consists of iron-loaded concrete blocks with layers of boron-loaded polyethylene and lead on their inside faces.

The QDQ has a momentum resolution, $\Delta p/p$, of $<0.15\%$ and a solid angle, $\Delta\Omega$, of 17.2 msr.

5.3 The deuterium target

A liquid-deuterium target was used for the experiment with HARP. It has a zero-current thickness of $\approx$235 mg/cm^2 and was designed to sustain electron beam currents of up to 20μA [Kasd97].

The liquid is kept at 20.8K by utilising a closed loop of deuterium which is cooled using a copper heat exchanger. The flow is maintained by convection; the cooling by the heat exchanger at one stage in conjunction with the heating up process caused by the electron beam at another. The target is illustrated in figure 5.5.

5.4 The data acquisition system and electronics

The relevant coincidence data from HARP and the QDQ spectrometer are collected, correlated and stored by the EMIN data acquisition system which has been briefly mentioned in section 3.2.

A trigger from the QDQ detector arm (an Arm Trigger, ATR), is sent to

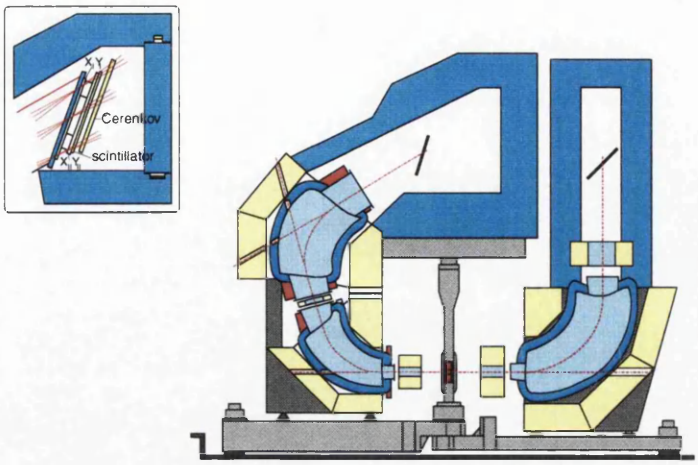

Figure 5.3: *The spectrometers in the EMIN hall. A QDD spectrometer is shown on the left with the QDQ spectrometer on the right. Inset is a view of the QDD internal detectors. The QDQ configuration is shown in figure 5.4*

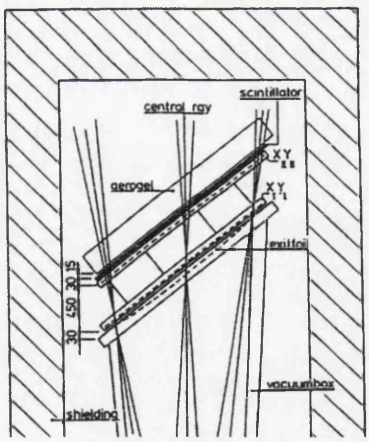

Figure 5.4: *The internal workings of the QDQ spectrometer. Illustrated are the wire-chambers and scintillator bars discussed in section 5.2. An aerogel detector is also illustrated. This is used for the detection of pions.*

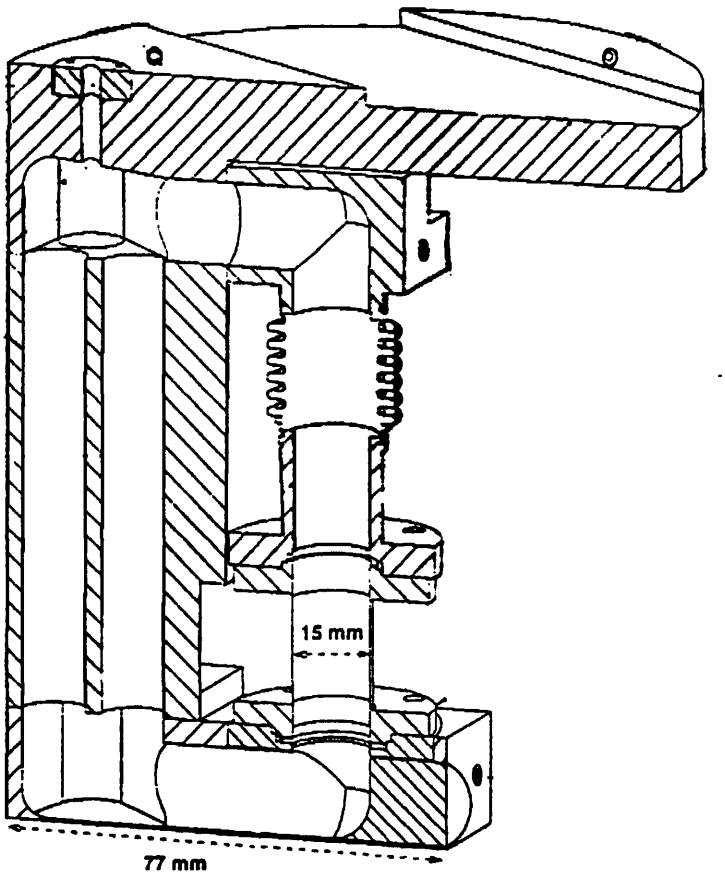

Figure 5.5: *A cross-section of the liquid deuterium target used in the experiment.*

a set of VME modules which act as a coincidence detector. These modules determine the time of arrival of the triggers and a General Purpose Module (GPM) is used to determine the type of event; a coincidence event between HARP and the QDQ spectrometer is based on the arrival time of the respective ATRs. A schematic overview of the coincidence logic is illustrated in figure 5.6

For the ^{2}H$(e, e'\vec{n})$ experiment, only coincidence events were selected, with single events of the QDQ and HARP ignored. These final events consist of the coincidence information as well as information covering the type of event and information unique to each detector.

5.5 Overview of kinematics

An overview of the experimental set-up is illustrated in figure 5.1. The ^{2}H$(e, e'\vec{n})$ experiment is performed in the quasi-free kinematical region with an expected electron beam of 600MeV and current of $1.5\mu A$. HARP is fixed in one position at $\theta_n = 45.0°$ and the energy of the incoming neutron predicted to be $\approx 150MeV$. A list of the other experimental parameters (as illustrated in figure 2.2) are given in table 5.1.

5.6 Summary of experiment

The experiment took place during the months of October and November in 1997 where a period of two weeks was allocated for data taking. Initial

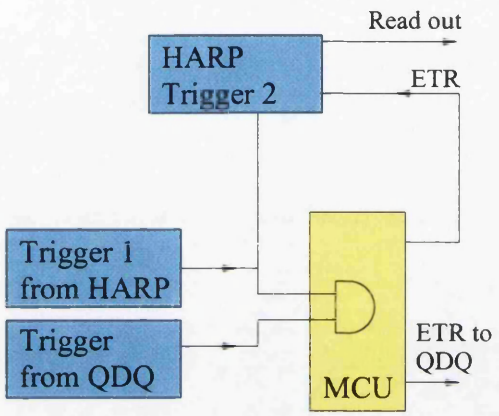

Figure 5.6: *Simplified scheme of the coincidence logic. ATR signals are sent to the master coincidence unit (MCU) which issues an event trigger (ETR) back to the detector arms if a coincident event is deemed to have occurred. Consequently each arm and the MCU unit send their responding event fragment to the Event Builder (EB) which merges the information fragments for storage.*

preparations installing HARP and the new data acquisition software required for this detector went well. During this preparation time, the wire-chambers were continually flushed with the Argon/Methane mixture to ensure the purity of the gas inside the chambers.

Data taking during the experiment was stored to computer disk for online analysis as well as to exabyte storage media for in-depth offline analysis at a later time.

Since this was the last scheduled external beam experiment, technical support was less available than normal. A poor quality beam from the start meant that data-taking was much slower than expected with beam currents (when available) fluctuating between $0.5\mu A$ and $2.0\mu A$. The quality of the beam also had a knock-on effect on the wire-chambers, causing sparking and tripping. This eventually led to one wire-chamber being damaged and unusable during the latter half of the data-taking period. The experiment finally came to an early end with the permanent failure of the beam.

Although the quality and quantity of the data taken was less than planned, it was decided that analysis of the data could still provide some useful results. This analysis is covered in the following chapter.

Parameter	Value	Parameter	Value
E_{beam}	600 MeV	E'	447.78 MeV
θ_n	45.0°	$\theta_{e'}$	60.6°
q	551.7 MeV/c	ω	152.2 MeV
θ_q	45.0°	$\mathbf{p_m}$	0.0 MeV/c
E_{np}	73.5 MeV	θ_{np}	180.0°
Time	116 hrs (planned)	Rate	30k events/hr. (planned)

Table 5.1: *Overview of kinematics for the* $^2H(e, e'\vec{n})$ *experiment.*

Chapter 6

Data Analysis and Results

The analysis of data obtained in the experiment detailed previously is presented in this chapter. The calibrations of data from the two detector arms, HARP and the QDQ spectrometer, are described separately: the calibration of the QDQ spectrometer is given in section 6.1 and the calibration procedure and analysis of the HARP detector is given in section 6.2. This information is then combined and coincidence analysis performed using information from both detector arms; this is discussed in section 6.3.

The data comes from the ^{2}H$(e, e'\vec{n})$ experiment which was run over a two week period. During these experiments, a failed wire-chamber meant that there was a severe restriction on the determination of particle tracking within HARP. To compound this problem, and with more serious implications, the beam stretcher ring at NIKHEF developed problems which meant that the amount of beam time available for real data taking after the necessary tuning of the detectors, was vastly reduced to only 4 hours. In addition, the quality of the beam for these 4 hours was severely reduced. The nature of the problem with the accelerator [1] was such that repair was impossible and use of the external beam at AmPS was permanently halted (since this was the last scheduled external beam experiment). This severe problem meant that the experiment could not be extended.

To circumnavigate the problem with the wire chambers, a method to track the scattering nucleons within HARP was developed using only information from the scintillator telescopes. This novel method is explained in

[1] The problem with the accelerator was due to the kicker breaking down beyond repair.

section 6.3.2. The second problem could not be overcome, severely limiting the number of coincidences taken, and its implications on the analysis are presented in the concluding sections of this chapter.

6.1 QDQ analysis

The QDQ spectrometer is used to detect the electron scattered from the primary target. The positional information from the multi-wire drift chamber (MWDC) planes is used to determine the track of the incident particle. Hence the particle's momentum and initial direction from the target can be obtained using the known [Vrie84, Vrie90] optical properties of the spectrometer.

An analysis package, GLANCE (General on-and-off Line ANalyser for Coincidence Experiments), developed at NIKHEF for electron scattering experiments, was modified to incorporate the HARP detector. This modified package, known as HARPGLANCE, interprets the raw information from the QDQ and HARP detectors and reconstructs the physical observables from the data (such as electron vector momenta, energies, event times as well as raw ADC and TDC information for the HARP detector) and presents these in useful output files for further analysis [2].

Using this information about the scattered electron, the angle and acceptance of the HARP detector and knowledge of the incoming beam energy, it is possible to determine the energy, ω, and momentum, $\mathbf{q}$, transferred to the

[2] ntuple files for use with the PAW analysis package.

target by the virtual photon and hence the kinetic energy, T_N, and momentum, $\mathbf{P_N}$, of the nucleon entering HARP. A spectra of the incoming neutron energy determined using the QDQ analysis and relevent trigger conditions within HARP is shown in figure 6.1.

Knowledge of the properties of this nucleon entering HARP is vital for calibrating HARP and proceeding with further analysis of the ^{2}H$(e, e'\vec{n})$ data.

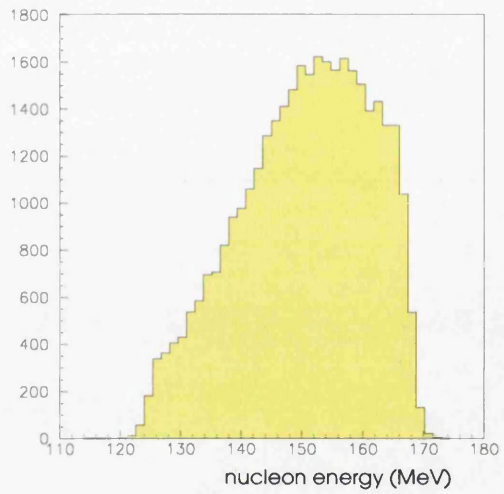

Figure 6.1: *The energy of neutrons entering HARP determined from analysis of the QDQ information and the kinematics of the $^2H(e, e'\vec{n})$ reaction.*

6.2 HARP analysis

Before any analysis of the experimental data can be made, it is important to calibrate HARP so that useful quantities can be extracted from the raw (TDC and ADC) information measured with this new detector. Inside HARP each

scintillator must be calibrated so that the hit location and energy deposit of a proton passing through the scintillators can be accurately determined. The methods to achieve this are described in sections 6.2.1 and 6.2.2.

Following this, the definition of valid events within HARP must be determined. This must be done by removing any spurious information while loss of genuine events is kept to a minimum; this is discussed in section 6.2.3.

Scintillator detectors use the luminescence property of certain materials (known as phosphors) which emit a small burst of light when a nuclear particle interacts with it and causes ionisation. When a particle impinges on these materials a fraction of the energy dissipated in molecular excitation and ionisation is re-emitted as visible or ultra-violet photons.

These small flashes can be amplified using photomultipliers and converted into electrical pulses that can be read using conventional electronics. The analysis of these photomultiplier signals is required to calibrate the position and energy of a particle passing through the HARP scintillator array. This process is covered in the following sections.

6.2.1 Position calibration

The position of an event in the scintillator telescopes can be obtained from the timing information gained from such an event. The relative time of registering an event at either end of a scintillator is performed using Time-to-Digital Converters (TDCs).

If we consider a charged particle passing through an individual telescope

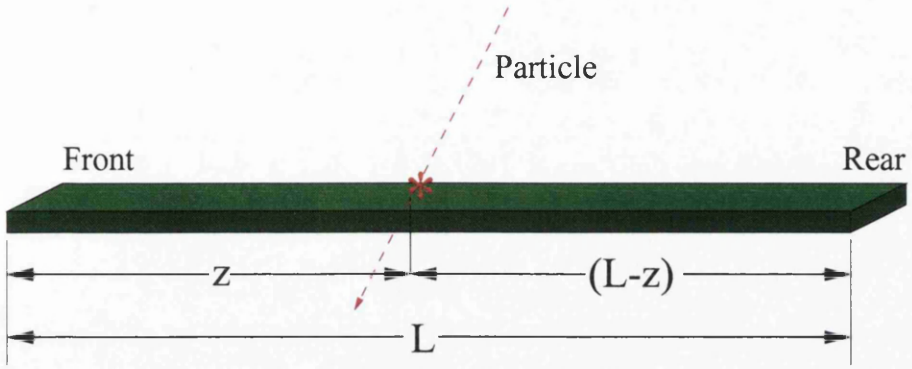

Figure 6.2: *The hit position, z, in a scintillator bar of length L.*

of length, L, at a distance, z, from the front end (figure 6.2), then the time the light from the scintillation process needs to reach either end of the telescope will be:

$$t_{front} = t_0 + \frac{z}{c'} \tag{6.1}$$

$$t_{rear} = t_0 + \frac{L - z}{c'} \tag{6.2}$$

where t_0 is a base time against which t_{front} and t_{rear} are measured, and c' is the speed of propagation of a light pulse in the scintillator plastic.

If we consider the difference between these, we can obtain a measurement of the position of the event interaction:

$$t_{diff} = (t_{front} - t_{rear}) = \frac{2z - L}{c'} \tag{6.3}$$

This value must be calibrated to fit the length of the scintillator telescope

and can be done by fitting the data to:

$$z_{corrected} = a \cdot (t_{front} - t_{rear}) + b \tag{6.4}$$

where $z_{corrected}$ gives the true hit position in the telescope measured in centimetres and a and b are calibration parameters.

These calibration parameters are found by demanding a coincidence in each telescope and fitting the spectra of these coincidences to the known length of each bar. This calibration is done independently for all scintillator bars. The result of this fitting technique is illustrated for one bar in figure 6.3 with the calibration parameters for all telescopes given in table 6.1. Whereas the "shift" parameters vary strongly (which is understandable since they correspond to abitrary cable delays) the "scale" factors are fairly consistent for each type of detector. The differences seen in the scale factors for the E and the M or D detectors are due to the longer effective pathlength of the light in the thinner detectors since more reflections are required.

6.2.2 Energy calibration

The different steps required to calibrate the energy deposit in the scintillators is presented here. The sections first describe the method by which a measurement of the energy can be obtained and a brief description of some corrections which were required. Before performing the actual calibration, it is necessary to determine the interaction vertex of the secondary scattering process in the liquid hydrogen converter. The interaction vertex is required so

	Scale (a) cm ns^{-1}			Shift (b) cm		
Telescope	E	M	D	E	M	D
1	0.267	0.308	0.283	340	240	240
2	0.258	0.302	0.281	260	300	260
3	0.267	0.305	0.296	300	125	250
4	0.250	0.302	0.296	250	310	260
5	0.276	0.296	0.283	340	260	325
6	0.271	0.302	0.291	220	230	250
7	0.276	0.296	0.281	260	220	300
8	0.267	0.296	0.286	340	240	240

Table 6.1: *HARP scintillator position calibration parameters. These are the "scale" and "shift" parameters ("a" and "b" in equation 6.4) per scintillator. As before, E, M and D represent the scintillator telescope layers, with E being the thickest at the rear and D the thinnest at the front.*

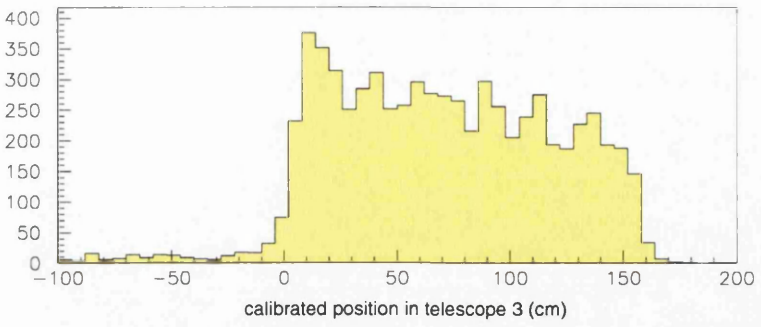

Figure 6.3: *Position spectrum for telescope 3, bar M. The spectrum has been shifted and calibrated to coincide with the length of the scintillator bar (160cm).*

that the path of the secondary scattered proton can be accurately described and hence the angle and distance traversed in the scintillator determined. After a method to achieve this is given, the final calibration of the energy deposit in the HARP scintillators is described.

Pedestal subtraction

As mentioned earlier, the pulse-height gives information on the energy deposit in the scintillator. The energy deposit in each scintillator is obtained by charge integration using Charge-to-Digital Converters (QDCs). The gating circuit for the QDCs causes a constant offset which is roughly proportional to the gate length [3], even when no event has been accepted. This offset is known

[3] other effects such as DC offset or too high a count rates can lead to varying offsets also.

as 'pedestal', and this pedestal value must be accounted for when using the measurements of the QDCs. When a pulse from an event is measured, the true pulse height (PH) can be extracted by subtracting the pedestal from the QDC value:

$$PH_{corrected} = QDC - pedestal \tag{6.5}$$

The pedestal is determined by looking at the QDC value of a telescope when no charged particle is deemed to have passed through [4]. The spectra of many such measurements are collected, from which the residual charge present in the QDC is measured.

Energy deposit reconstruction

For a charged particle interacting in a plastic scintillator, the total light output from the scintillation process is not strictly proportional but has a relationship with the energy deposited that can be expressed in the form [Cecl79]:

$$\mathcal{L}(\mathrm{E}) = \alpha \mathrm{E} - \beta(1 - \exp(-\gamma \mathrm{E}^{\delta})) \tag{6.6}$$

where $\mathcal{L}$ is the total light output, E is the incident particle energy and $\alpha, \beta, \gamma, \delta$ are particle and scintillator medium dependent parameters. Using this relationship it is possible to determine the energy deposited in the scintillator from the light output measured once these 4 parameters are known.

[4] for example, one can require a hit in telescope i and no hit in the TDCs of telescope j (i≠j) to look at the pedestals of the PMTs in telescope j.

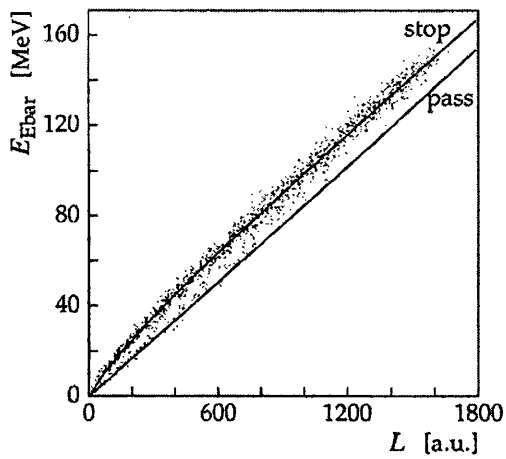

Figure 6.4: *Light output (x-axis) as a function of incident energy (y-axis) in scintillator material. [dBok86].*

Light output from low energetic particles stopping in the scintillator material suffers from a quenching effect which originates, essentially, from the saturation of the high local density of ionisation surrounding the region where the particle stops. This quenching effect depends on particle mass; for protons it causes equation 6.6 to become significantly non-linear at incident energies less than ~10MeV (and is visible in the HARP scintillators upto ~80MeV). In addition it causes the relationship to differ for particles stopping in the scintillator material and those passing through (see figure 6.4), since the former cause saturation whereas the latter produce much less ionisation over pathlength.

To determine the energy deposited in a scintillator by an incident proton,

the parameters for the relationship between light output and incident energy must be determined using only the linear range in equation 6.6. This must be found for the different cases where protons stop and pass through the scintillator respectively.

Energy deposit measurement

For the scintillator bars in HARP, the light pulses (generated by an interaction within the scintillator material) are read out at both ends of the bar using PMTs. The light is attenuated on its path from the impact position to the cathode of the photomultiplier. For the material used in the HARP scintillators (Bicron 400) the attenuation length is $2.4m$. The geometry of the scintillator also contributes an effect but an exponential attenuation is assumed. When corrected for the intrinsic pedestals, the measured pulse height at the front and rear of the scintillator bars can be expressed as:

$$PH_{front} = c \cdot \mathcal{L} \cdot \exp\left(\frac{-\mathrm{z}}{\lambda}\right) \tag{6.7}$$

$$PH_{rear} = c \cdot \mathcal{L} \cdot \exp\left(\frac{-(\mathrm{L}-\mathrm{z})}{\lambda}\right) \tag{6.8}$$

where c is a constant, λ is the attenuation length, $\mathcal{L}$ is the total light output, z is the position of impact and L is the length of the scintillator bar.

The total light output for a scintillator bar can be found by measuring the pulse height at either end and taking the square root of the product.

$$QDC_{front} \cdot QDC_{rear} = c^2 \cdot \mathcal{L}^2 \cdot \exp\left(\frac{-\mathrm{L}}{\lambda}\right) \tag{6.9}$$

$$\sqrt{QDC_{front} \cdot QDC_{rear}} = constant \cdot \mathcal{L} \tag{6.10}$$

Thus taking the square root of the product of the front and rear QDCs gives a measurement which is independent of the hit position. In addition, we are now able to determine a measurement which is proportional to the total light output, $\mathcal{L}$, and hence proportional to the energy deposit, E. The relationship between this measurement of $\mathcal{L}$ and the actual E deposit can then be determined after some corrections which are explained in the following sections.

QDC corrections

If the pulse height measurement attenuation is not perfectly exponential then the geometrical mean ($\sqrt{QDC_{front} \cdot QDC_{rear}}$) will exhibit a small dependence on the hit position in the telescope. This additional effect is known as 'droop'. The 'droop' effect in the HARP scintillators was found to be negligible and is not taken into account in the analysis.

A failing PMT at one end of one of the telescopes (telescope 6M) meant that, for this scintillator telescope concerned, an alternative method to determine the total light output had to be found. By taking the ratio of the pulse heights measured at the front and rear ends of scintillator telescope, it is possible to obtain a function independent of $\mathcal{L}$:

$$\frac{PH_{front}}{PH_{rear}} = exp\left(\frac{L-2z}{\lambda}\right) \tag{6.11}$$

By plotting the ratio of the front and rear pulse heights of the remaining

telescopes against the hit-position, it is possible to determine the attenuation length, λ, from the slope of the graph (the value of this ratio at hitposition $z = L/2$ gives the relative gains of the front and rear PMTs). Each telescope is of identical design and so λ should be equal for all scintillator bars of the same type. Table 6.2 shows the values of λ for the M layer for each of the other telescopes. A value of $-9.0 \pm 0.8 \times 10^{-3}$ was taken for λ_{M6} using these calculated values as a basis for determining the unknown quantity.

Using this value of λ, a value for the non-functioning front PMT pulse height was determined using the pulse height measured at the rear PMT, the known length, L, of the scintillator bar and the hit position, z, calculated using the TDC information:

$$PH_{front} = PH_{rear} \cdot exp\left(\frac{L - 2z}{\lambda}\right) \tag{6.12}$$

Calibration in MeV

With a satisfactory measurement of a quantity which is proportional to the energy deposited in the scintillator medium, it is necessary to find the ratio between this measured value and the actual energy. This ratio provides the calibration factor that enables one to know the energy deposited from the electronic measurement. To find this ratio it is necessary to take a series of measurements where the incident particle's energy is known and observe the measured electrical photomultiplier pulse so that a correlation between these two values can be ascertained.

The reaction, $D + e \longrightarrow e + p + n$, is kinematically defined once the

Telescope	λ (cm)
1	-9.0 $\times 10^{-3}$
2	-8.5 $\times 10^{-3}$
3	-8.1 $\times 10^{-3}$
4	-8.2 $\times 10^{-3}$
5	-9.8 $\times 10^{-3}$
6	-9.0 $\times 10^{-3}$
7	-8.8 $\times 10^{-3}$
8	-10.8 $\times 10^{-3}$

Table 6.2: *Calculated values for the attenuation constant (λ) for the M layer of each of the telescopes.*

incoming and outgoing momentum vectors of the electron and the direction of one of the nucleons is known. With knowledge of the electron's momentum vectors and the in-plane angle of the nucleon detected in HARP, the out-of-plane angle of the nucleon does not affect the precision of the kinematics more than a few MeV in the energy of the nucleon. This argument is true so long as pion production is excluded. In this experimental case, the electron's incoming and outgoing energy would allow the production of a pion only when the nucleons' energies are below around 25MeV. This 25MeV is below HARP's detection threshold and so such events will not be present in the experimental data.

With the incoming nucleon energy determined from the QDQ analysis, it is possible to track this nucleon through HARP and calculate what energy it should have when it hits the scintillators after scattering in the LH_2. However, without the information of the wire-chambers, retracing this track is not straightforward. Although the hit position in the scintillator may be known, the interaction point within the LH_2 vessel and the scattering angle remains undetermined and hence the energy loss of the incoming nucleon as it passes through the LH_2 cannot be calculated. A method to overcome this difficulty was devised using $(p, 2p)$ events within HARP and a helpful property of this reaction.

Determination of interaction vertex in the converter

The limitation caused by the failing wire-chambers meant that the determination of the interaction position in the converter needed to be obtained in

another manner. Although HARP is primarily a neutron detector, analysis of incoming proton events provided such a method.

At energies below ~500 MeV, the opening lab angle between the two nucleons leaving the converter is $\approx \pi/2$ radians [5] (see figure 6.6). If the incoming nucleon is a proton, then it is possible to detect both this scattered and the recoiling protons scattered from the liquid hydrogen in coincidence in the left and right scintillator banks.

Using the scintillator hit position information for $(p, 2p)$ events within HARP it is possible (see figure 6.7) to find the z-coordinate of the interaction vertex within the LH_2 vessel using simple geometry:

$$z_0 = \frac{z_1 + z_2 - \sqrt{z_1^2 + z_2^2 - 2z_1 \cdot z_2 + 4y^2}}{2} \tag{6.13}$$

where z_0 is the z-coordinate of the reaction vertex within the LH_2 vessel and z_1 and z_2 are the hit positions in the z-plane in the scintillator telescopes on either side of the converter. Here an opening angle of $\pi/2$ is used.

The detection of two coincidence events in scintillator telescopes that are symmetrically opposite (see figure 6.5) in addition to a coincidence in the charged particle tagger provided an almost perfect detection coincidence condition for 2 proton events within HARP. Using these criteria provided great confidence in the determination of the reaction vertex.

Background caused by protons scattering from the LH_2 frame is minimal because the scattered protons lose so much energy that the detection of both

[5] at $T_p = 200MeV$, the maximum deviation from $\pi/2$ is about 3°

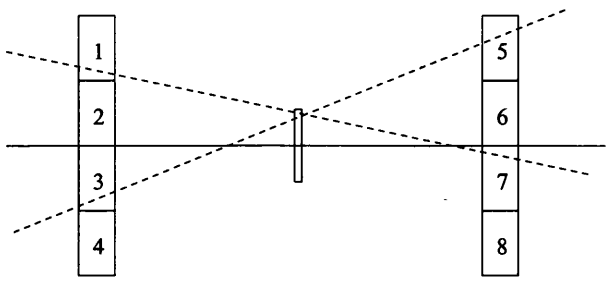

Figure 6.5: *A front-on view of the $(p, 2p)$ events within HARP with the converter vessel in the centre and the scintillator telescopes on either side. The dashed lines represent possible proton tracks leaving back to back from the LH_2 (the incoming proton and the scattered proton leave the LH_2 vessel at the azimuthal angle, $\Phi = \pi$ radians). The size and position of the vessel means that $(p, 2p)$ events are only valid if a line tracing these 2 proton tracks can be drawn through the LH_2 vessel and the corresponding telescopes (e.g. the dashed lines in the figure). From this figure it can be seen that a hit in telescope 1 requires a corresponding hit in telescopes 7 or 8 on the opposite side of the converter. A hit in any other telescope with telescope 1 is not possible from the same $(p, 2p)$ event within the LH_2 and so can be used to veto background from the frame.*

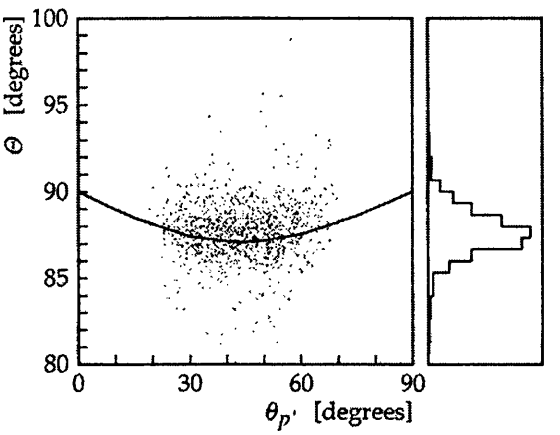

Figure 6.6: *Angular correlation between proton tracks in* $(p, 2p)$ *scattering events inside HARP. The opening angle* Θ *is plotted as a function of the recoil angle of one of the two protons [dBok86]. The incoming proton energy is 200MeV.*

protons on either side in coincidence is highly unlikely.

Figure 6.8 shows the reaction vertex positions gained using the above method for a number of events. The plot reflects the length of the vessel well which indicates a realistic method for determining the z-coordinate of the reaction vertex. It is noteworthy to observe that the intensity diminishes the further the interaction vertex is from the front of the converter. One might expect the intensity to reduce as the diminishing solid angle with distance between target and vertex within the LH_2 vessel. It appears that this is not entirely the case from the plot however the shortage of statistics makes this difficult to ascertain.

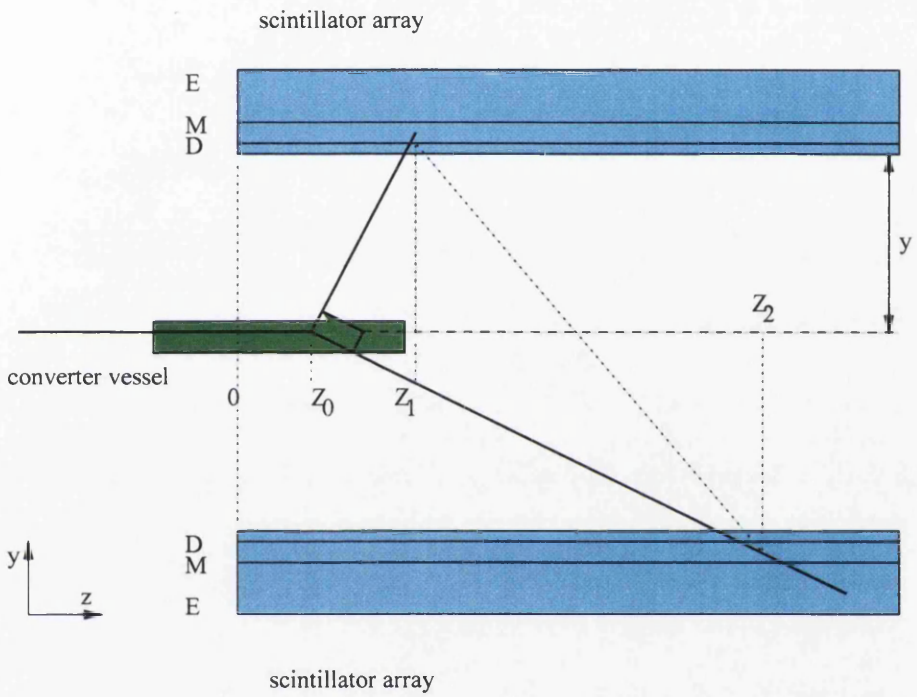

Figure 6.7: *The geometry of $(p, 2p)$ events within HARP. Using the hit positions in the telescopes on either side of the converter and the opening angle between the recoil and scattered proton, the interaction point inside the converter can be determined.*

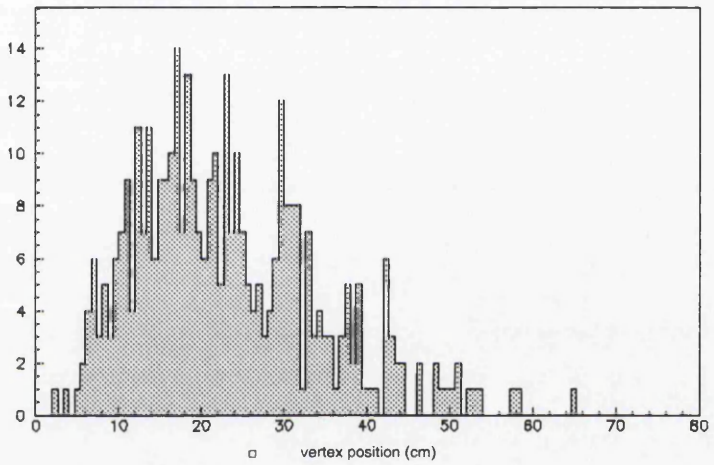

Figure 6.8: *The z-coordinate of the interaction vertex within the LH_2 vessel shifted so that 0 represents the front of the converter. The vertex distribution coincides well with the length of the LH_2 converter of 60cm.*

QDC-MeV calibration

With a method to determine the reaction vertex using incoming proton events verified, the energy calibration of the telescopes could be carried out using the same data.

Once again, $(p, 2p)$ events were selected within HARP by requiring a single unambiguous hit in a telescope on either side of the converter coupled with a hit in the charged particle tagger.

The incoming proton energy, T_p, is known from the QDQ analysis (as outlined in section 6.1) and from the hit position in each telescope, the recoil proton angles and reaction vertex in the converter were determined as illustrated in the previous section.

Using the interaction vertex within the LH_2, the proton scattering angles and our knowledge of the incoming proton energy, the energies of the secondary protons emerging from the interaction vertex can be determined. First, the energy loss of the incoming proton as it passes through the dead material within HARP is calculated up to the interaction vertex position in the converter. This depleted energy proton (with kinetic energy T_p^0) then undergoes elastic scattering with another proton in the converter and each scatters at a different angle where they are detected by the arrays of scintillators on either side. The scattered protons have an initial energy (neglecting small relativistic effects) given by:

$$\begin{aligned} T_p^1 &= T_p^0 \cdot cos^2\theta_1 \\ T_p^2 &= T_p^0 \cdot cos^2\theta_2 \end{aligned} \tag{6.14}$$

where T_p^0 is the incoming proton energy at the interaction point in the LH_2 vessel, T_{p1} and T_{p2} are the calculated energies of the scattered protons just after the reaction and $\theta_{1,2}$ are the scattering angles.

The energy losses for these secondary protons are again calculated as they leave the converter until they are detected in the scintillator telescopes. The energy deposited in each scintillator is then calculated and compared to the measured values obtained from the QDCs. The ratio of the *expected* and *measured* energy deposit from these $(p, 2p)$ events allows one to obtain a calibration factor by which the measured energy from the QDCs can be converted into the actual energy deposited.

6.2.3 Event selection

The determination of a valid event within HARP is important so that spurious noise can be reduced. A valid hit within HARP is deemed to have occured with the detection of a proton in one of the scintillator telescopes. A proton knocked out of the liquid hydrogen converter will pass though the D layer scintillator and either stop in the M or E layer depending on its energy and angle of incidence. A proton stopping in a telescope will always pass through at least 2 scintillator layers in that telescope. A valid hit is therefore defined as a hit in two consecutive scintillators in a telescope (i.e $DM\bar{E}$, $\bar{D}ME$ or DME)[6].

[6]For notational purposes, a detected event in a particular telescope is represented by the scintillator layers letter (given in section 3.1.3) with a non measurement represented

Furthermore, windows [7] placed on the HARP scintillator TDC and QDC information reduce the amount of irrelevant data and restrictions on events in the HARP telescopes are made to ensure that they originate from the LH_2 vessel. The restrictions applied used rough particle tracking from hit position information in successive scintillator layers to veto events that could not have originated from the converter vessel.

Information from the tagger strips is used to veto unwanted incoming particles or to discriminate between incoming protons and neutrons. A hit is defined as an incoming proton when a corresponding pair of tagger strips from the front and rear layers fire; an incoming neutron is defined when no tagger strips fire. The charged particle tagger array, previously shown to operate with a detection efficiency of greater than 99.9% [Munz96], provides good confidence that the identification of the incoming nucleon is known.

More stringent event selection conditions can be added which improve the ratio of valid to accidental events. One such condition that was successfully applied was the requirement that the hit-positions of the recoil nucleons as they passed though successive layers of the scintillator telescopes should be such that backward angle path events were ignored. This is achieved by requesting that events detected in the scintillator telescopes are in a forward line through consecutive layers (i.e the hit position in the E layer must be

by an overstrike so that $DM\bar{E}$ indicates that an event was measured in layers D and M but nothing was detected in the E layer.

[7] upper and lower threshold limits on electronic signals

further from the front of the detector than hit position in the M layer for the same event).

Other improvements were made when re-analysing the data at a deeper level. These additional improvements, allowing a much cleaner data-set included:

- for incoming neutrons, only one non-ambigous event is detected by the scintillators in addition to the null event detection of the charged particle tagger.
- cuts are applied to the energy deposited in the scintillators so that background events are ignored.

The dark overlaid prompt in figure 6.10 shows this much improved event selection: the majority of accidental events have been removed without the loss of too many valid coincidences.

The detection of the scattered electron in the QDQ spectrometer in coincidence with the HARP telescope hit gives a very clean definition of a good event, and this is discussed in section 6.3

6.3 Coincidence analysis

In the following sections the information from both HARP and the QDQ spectrometer are combined to perform the coincidence analysis proper. The definition of what constitutes a valid coincidence between these two detector arms is given in section 6.3.1. Section 6.3.2 then discusses a more detailed

analysis of the ^{2}H$(e, e'\vec{n})$ data and the methods employed to determine the secondary scattering angles, the corrections due to "dead material" within HARP and then the final calculations made to obtain a measurement of the asymmetry.

6.3.1 Timing coincidence

To perform coincidence analysis, it is first useful to look at the hardware events that are measured in coincidence between the QDQ spectrometer and HARP. The Coincidence Detector (CD) electronics detects simultaneous events in the QDQ and HARP by placing a time window on the differences of the ATR signal arrival times.

These coincident events comprise of both genuine and accidental coincidence events (i.e. events originating from the same microscopic interaction as well as events from different interactions which occur independently to each other but at roughly the same time). The histogram in figure 6.9 illustrates the timing distribution of these genuine and accidental coincidences. The random nature of the accidental coincidences allows us to recognise the true events from the distinct *prompt* peak in the spectrum.

This raw peak allows one to further refine the data so that only genuine events are analysed. After all other cuts have been made within HARP and the QDQ, a cut is made on the time difference so that only events which fall within the correct time (marked by the prompt) are selected. The timing peak itself can also be improved before it is used as a basis for event

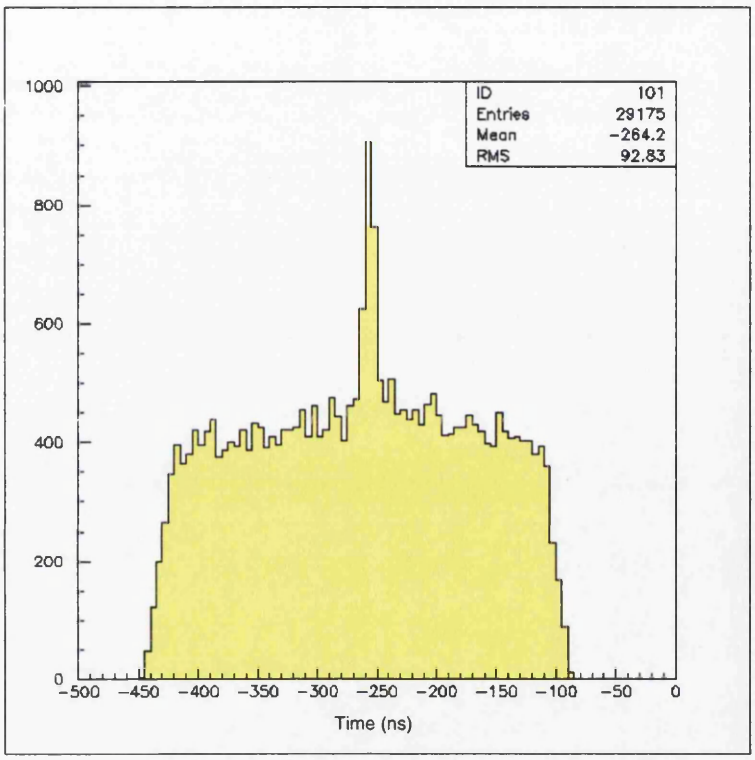

Figure 6.9: *Timing coincidence between the QDQ spectrometer and HARP. The histogram shows the raw timing coincidence before any cuts on the HARP scintillators have been applied.*

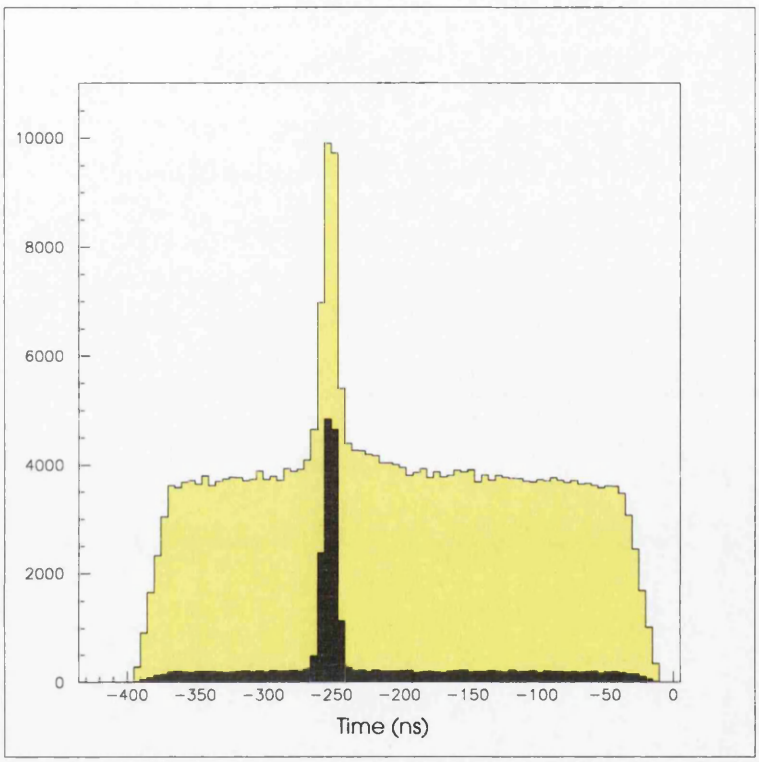

Figure 6.10: *Timing coincidence between the QDQ spectrometer and HARP. The light grey histogram shows the raw timing coincidence before any cuts on the HARP scintillators have been applied. The dark histogram projected in front shows the coincidence spectrum after placing loose conditions on HARP scintillator information.*

selection and this is done using the analysis software. An overview of these improvements is given next.

Timing corrections

The raw timing prompt in figure 6.9 has a Full-Width Half-Maximum (FWHM) of 14ns.

The difference in trigger times can be caused by a variety of effects including: 'walk dependence' and difference in electronic cable lengths and mean-timer delay effects.

The first step is to reduce the random background and this can be obtained easily by requiring that at least 2 adjacent scintillator layers in one telescope (DM or ME) have a narrow 4-fold PMT coincidence. The result of this cut is shown as the dark overlaid histogram in figure 6.10.

The major part of the spread is due to the different cable lengths and transit times in the PMTs between the HARP scintillator telescopes and the QDQ spectrometer. The peak in figure 6.10 shows the superposition of 8 different individual timing peaks between the scintillator telescopes and the QDQ spectrometer. These peaks can be shifted to one common position once their relative positions are known. This can be achieved by studying the coincidence timing between HARP and the QDQ when each individual telescope fires and adding a timing shift parameter to align each telescope time signal.

The 'walk' effect influences the trigger timing and hence the timing res-

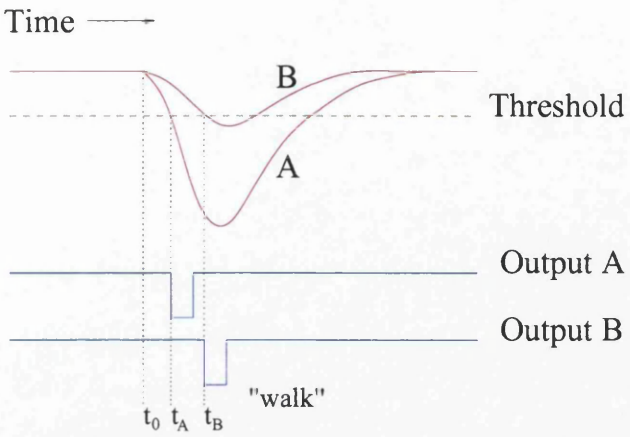

Figure 6.11: *The 'walk' effect observed when coincidence signals of different amplitudes that start at the same time have different trigger times.*

olution of coincidences between HARP and the QDQ spectrometer. This effect is caused by coincidence signals of different amplitudes which may start at the same time, but do not trigger a detection event at the same time due to the differing times when the signals cross the disciminator threshold (see figure 6.11).

Compensation for walk effects provided a small gain. However a considerable improvement to the timing resolution was made by compensating for the different delays between HARP telescopes due to the electronics and cabling. The improvement to the timing peak is illustrated in figure 6.12 where a full-width-half-mean (FWHM) of $1.6ns$ is shown.

With the improved timing prompt, one can make finer cuts on the data and be confident that valid events are retained while reducing background noise.

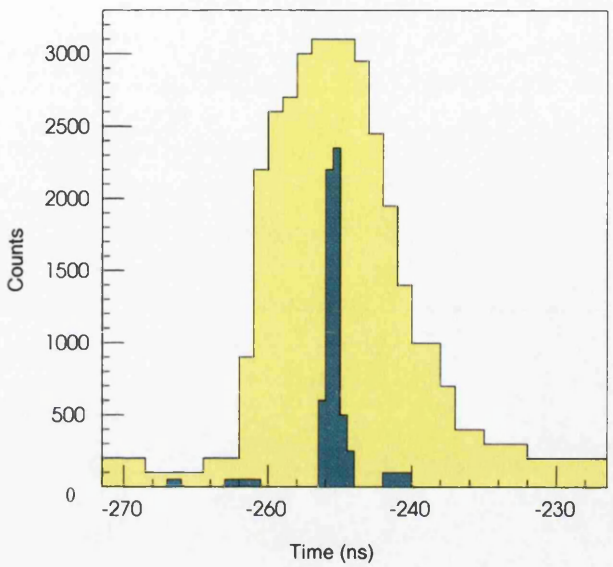

Figure 6.12: *The final resolution of the timing peak for coincidences between HARP and the QDQ spectrometer. The light peak in the background is the raw time with a FWHM of 14ns before any corrections (and with loose cuts to reduce background) are applied. The dark peak overlaid shows the corrected time resolution, after cable differences and walk effects have been compensated, with a FWHM of 1.6ns*

6.3.2 The recoil proton scattering angle

In the absence of wire chamber information, the alternative method to determine the recoil proton angles from nucleon scattering within HARP as described in section 6.2.2 has been used. Although detection of the scattered neutron in the stopping E bars was possible (and hence the possibility of using the hit-positions of both the scattered neutron and recoil proton detected in coincidence to determine the relative angles in a similar manner employed to obtain the QDC-MeV gain factors) a more reliable and statistically favourable method was envisaged.

This approach uses the fact that there is a direct correlation between the recoil proton's energy and scattering angle for a known incident energy. In order to study the influence of the detector material, Monte Carlo simulations were carried out.

Monte Carlo simulations

A Monte Carlo program is required to simulate the detector behaviour. For this task, the CERN GEANT software [Brun90] was modified to mimic the experimental environment. A large number of events were simulated for incoming neutrons with a range of energies and the energy deposited in the scintillator telescope banks for the secondary scattered proton from the LH2 vessel was calculated and plotted against its scattering angle. Figure 6.13 illustrates the strong correlation between these parameters and so gives a favourable indication towards the validation of this method.

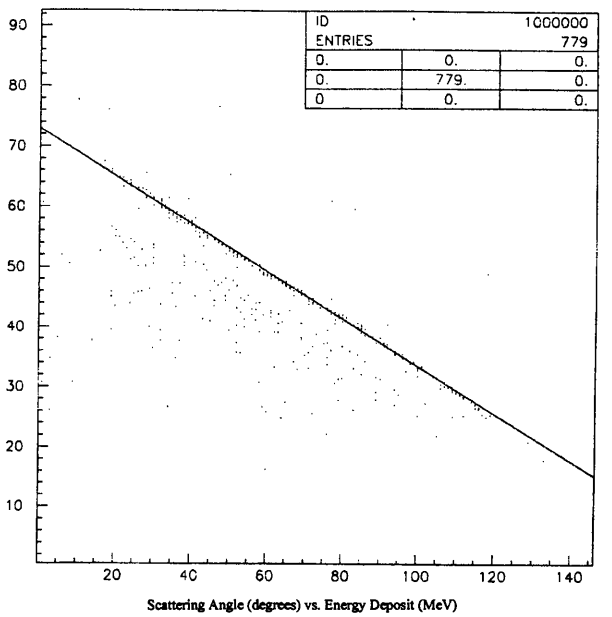

Figure 6.13: *The plot obtained from Monte-Carlo simulations shows the secondary scattering angle vs. the energy deposit measured in the scintillator telescope. The strong correlation between these parameters can clearly be seen (indicated by the overlaid line). Events below the line are caused by very high energy protons which pass right through the scintillator bars and so do not deposit all their energy.*

Determination of recoil and scattering angles

With the position and energy calibrations complete it becomes possible to determine the real position and energy deposit of the recoil proton within the HARP telescopes.

For incoming protons of a known T_p it is possible to calculate the energy loss at each stage as it passes through HARP. By stepping through the length of the converter in small increments (calculating the energy loss of the proton at each step) and using the relationship given in equation 6.14, a "look-up" table can be created mapping the recoil energy (and total energy deposit in the scintillators) with the recoil angle for 1cm steps along the converter.

By taking the hit-position and total energy deposit of a proton detected in a telescope, it is possible to "look-up" our table in the analysis software and interpolate between entries to deduce the scattering angle.

For incoming neutrons this method becomes even more reliable since the incoming neutron does not interact with the dead material as it enters HARP and so its energy at the interaction point within the converter can be assumed to be the same as that calculated for it when it left the primary target. A second "look-up" table was created for (n, np) events which allowed the recoil proton angles to be determined using only the measured hit position and calculated energy of the incoming neutron.

For both sets of "look-up" tables, the energy loss of the recoiling proton as it travelled between the interaction vertex in the converter and the scintillators was taken into account. A plot of the scattering angle obtained in

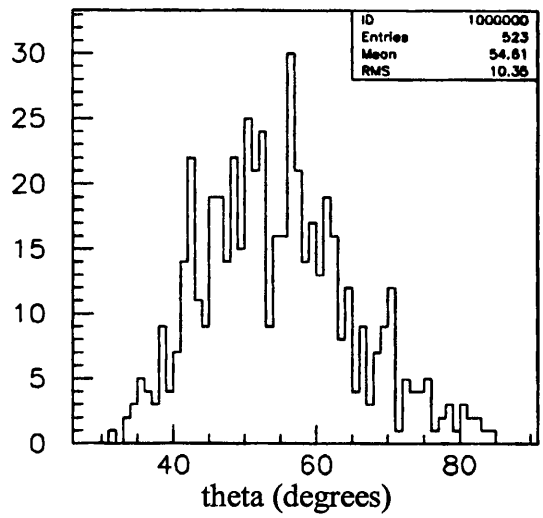

Figure 6.14: *The reconstruction of the secondary scattering angle within HARP using the hit position and energy deposit measurements from the scintillator and the known energy of the neutron entering HARP.*

this way is shown in figure 6.14.

6.3.3 Correction for background

In order to remove any background events in the analysis caused by events which did not originate from the LH_2 vessel (e.g. caused by the target walls or detector construction), it it necessary to analyse experimental data taken for the same kinematics but with an empty converter.

Normalising for the two sets of experimental data (full and empty converter) and looking at the difference allows one to obtain a more accurate picture of the interactions within HARP.

6.3.4 Calculation of P_0^y

The analysing power of n-p scattering at different energies has already been indicated in figure 2.8 and is non-constant for p-p scattering also.

Equation 2.23 gives the essential formula for extracting the polarisation of a beam of particles from a measurement of yields on either side (i.e. differing by an azimuthal angle of π) of a (secondary scattering) target and a known analysing power of the scattering process. From this it becomes clear that the shape of the analysing power plays an important role and a measurement in regions where $A_y = 0$ must be avoided. This implies also that the average of A_y must be non-zero and so a measurement in a region where A_y is large seems most preferable. This argument is too simple however, because the statistical uncertainty will be determined by the yields N_+ and N_-, repectively, which depend upon the underlying cross-section.

The optimisation of a polarimeter relies on the optimisation of the acceptance of the apparatus of the product $A_y \times d\sigma/d\Omega$. In principle, the extracted polarisation of the incoming particle beam must be independent of the secondary scattering angle. A large angular acceptance, such as is featured by HARP , can be used to verify this.

Since HARP can also be used to measure the polarisation of incoming protons, it is also an excellent apparatus to measure the analysizing power $A_y(\Theta)$ of the p-p scattering process.

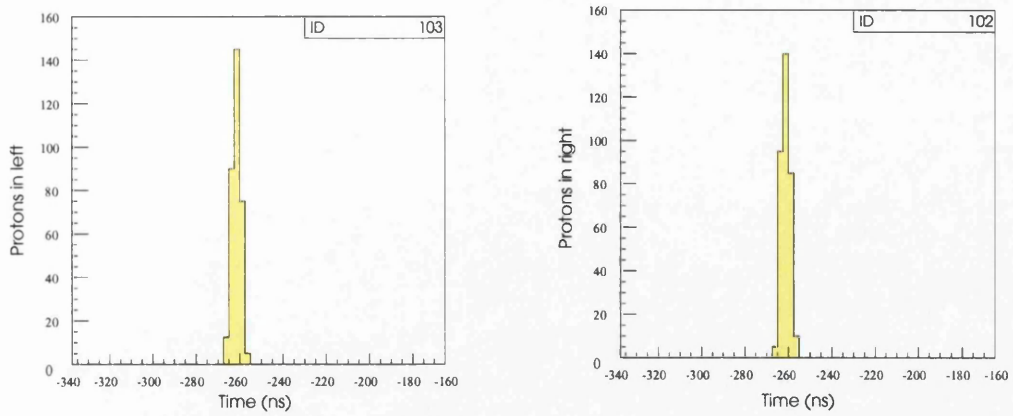

Figure 6.15: *The number of detected protons in each side of the detector before detector efficiency corrections are applied. "left" and "right" refer to the sides of HARP looking from the front (i.e. the right side is the side closest to the beam direction).*

6.3.5 Results of analysis

Using the "look-up" tables outlined previously, the secondary scattering angle, θ, was determined for the $^2\mathrm{H}(e, e'\vec{n})$ data (figure 6.14) but the extreme shortage of data meant that performing any analysis on the difference in scattering angle on either side of the converter vessel was hampered by the large statistical errors involved.

A value of 0.012 was determined for the asymmetry with a statistical error of ± 0.039 and a systematic error of ± 0.03 The error is almost entirely due to the shortage of statistics available.

If one bins the data by secondary scattering angle (θ) and incoming neutron energy (E) one can obtain a weighted value of 0.4 ± 0.02 for the

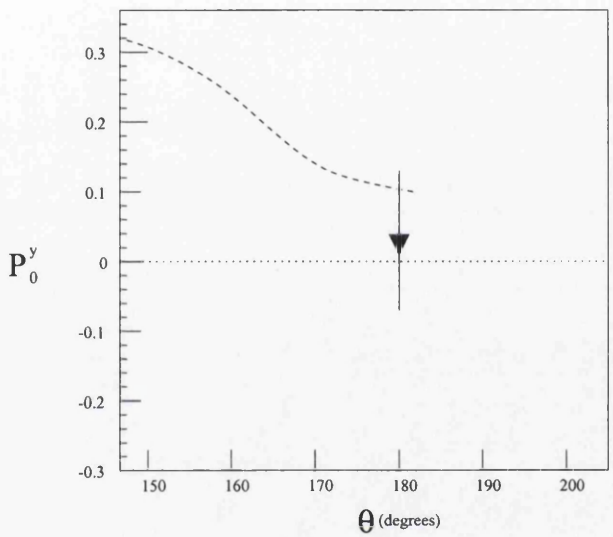

Figure 6.16: *Value of P_0^y including error bars calculated using a constant analysing power of 0.3. The dotted line represents Arenhövel's theoretical calculation (figure 2.4).*

analysing power. Using this figure, a value of 0.03 ± 0.1 can be obtained for P_0^y .

This is illustrated in figure 6.16 where this point is shown overlaying a dotted line representing Arenhövel's theoretical prediction.

It was calculated that 6.2×10^5 neutron events would be required to produce a result for P_0^y to within a 10% accuracy using the method employed here without the use of wire-chambers.

The analysis of the data taken during the $^2\mathrm{H}(e, e'\vec{n})$ experiment did, however, point to some positive aspects of the HARP detector. The scintillator arrays performed exceedingly well and, once calibrated for timing and position information, were able to be used in a method to self-calibrate the energy deposit within them. In addition, the study of the scintillators indicated that additional data could be extracted from their analysis including the reconstruction of the secondary scattering angles. In fact, only the lack of statistical data prevented this from being an interesting and informative method to measure the left-right asymmetry of the incoming neutron in HARP from the $^2\mathrm{H}(e, e'\vec{n})$ reaction. The analysis also highlighted the good timing resolution available with HARP, proving the detector to have the potential for obtaining good physical measurements.

While the physics results obtained from the $^2\mathrm{H}(e, e'\vec{n})$ experimental data suffered heavily from the lack of available statistics, the analysis of the little data that was available indicated a solid argument for the validity of HARP as a neutron polarimeter.

Chapter 7

Conclusion and the Future of HARP

The commissioning experiments with HARP showed that the detector system, in principle, operated as designed. The data acquisition system and general electronics performed the task required of them and the scintillator telescopes and charged particle tagger functioned well. The tagger reached 99.9% detection efficiency and a timing resolution of 1.6ns was seen for the HARP detector. The cryogenics system operated smoothly and safely and the wire-chambers, although operating at very low detection efficiencies, showed that they could be used to track the charged particle knocked out from the converter volume in the secondary reaction.

The failure of the wire-chambers during the $^2\mathrm{H}(e, e'\vec{n})$ experiment of November 1997 placed severe restrictions on the analysis of the data obtained. Problems with the electrostatic kicker of the electron accelerator during the experiment meant that the amount of available data was greatly reduced and this, coupled with the wire chamber failures, meant that the physics information that could be extracted from the data was insufficient. However, there were technological lessons from which much could be learned.

The scintillators making up the charged particle tagger and the larger detecting telescopes and their associated electronics performed well: proton detection efficiency was measured at 97% and a time resolution for the detector was determined as 1.6ns.

The HARP liquid hydrogen system operated stabily in a high lumonisity electron scattering environment. The HARP box was flushed with nitrogen gas and the monitoring process showed a stable oxygen content in the box

of less than 3% over the 3 week period.

Without the wire-chambers, the full capabilities of HARP were not realised. Various attempts to increase the chambers' robustness were not able to bring them up to the functionality required for the experimental environment. It is believed that mechanical flaws in their construction rather than their design caused their downfall.

In conclusion, the HARP detector was, disregarding the wire-chambers, shown to behave as expected and has shown itself here as a promising new detector. In addition, a novel method to analyse data using HARP without wire-chambers has been outlined in this thesis and, although lack of data prevented conclusive results to be drawn, the method itself shows promise.

Constructing MWPCs that are able to sustain the high rates required for the the $^2\mathrm{H}(e, e'\vec{n})$ experiment is possible and that if new MWPCs were fitted, HARP could function extremely well as a polarimeter.

The HARP detector has been shipped from NIKHEF to TJNAF in the United States to take part in new experiments.

Bibliography

[Alva40] L. W. Alvarez and F. Bloch,
Physical Review ***57****, (1940) 111*

[Aren88] H. Arenhövel, W. Leidemann and E. L. Tomusiak,
Z. Physik A - Atomic Nuclei ***331****, (1988) 123*

[Aren92] H. Arenhövel, W. Leidemann and E. L. Tomusiak,
Physics Review ***C46****, (1992) 455*

[Aren99] H. Arenhövel, W. Leidemann and E. L. Tomusiak,
nucl-th/9905029 (1999)

[Aren00] H. Arenhövel, F. Ritz and T. Wilbois,
Phys. Rev. ***C61*** *(2000) 034002*

[Arnd81] R. G. Arnold, C. E. Carlson and F. Gross,
Physics Review ***C23*** *(1981) 363*

[Asch94] E.C. Aschenauer et al.,
NIKHEF-K Electron Scattering Proposal NR:94-04

[Auff85] S. Auffret et al.,
Physics Review Letters 55 (1985) 1362

[Baue97] T.S. Bauer,
Private communication.

[Boer95] D. Boersma,
'Preliminary test of HARP scintillators.',
HARP internal report, Utrecht University, (1995)

[dBok86] H. den Bok,
PhD. Thesis, Utrecht University, (1996)

[Bern81] M. Bernheim et al.,
Nuclear Physics ***A365*** *(1981) 349*

[Blok93] H.P. Blok et al.,
NIKHEF-K Electron Scattering Proposal NR:93-2

[Boff95] S. Boffi et al.,
'Electromagnetic Response of Atomic Nuclei'
Oxford Studies in Nuclear Physics 20 (1995)
Clarendon Press, Oxford
& references therin.

[Brun90] R. Brun, F. Carminati, F. Bruyant, M. Maire,
*CERN Computer Newsletter****200*** *(1990) 13*

[Cecl79] H.A. Cecil et al.,
Nuclear Instruments and Methods ***161*** *(1979) 439*

[Chad32] J. Chadwick,
Nature ***15*** *(1932) 323*

[Chad34] J. Chadwick,
Nature ***15*** *(1934) 323*

[Char62] Charpak,
Nuclear Instruments and Methods ***15*** *(1962) 323*

[Fabi79] W. Fabian and H. Arenhövel,
Nuclear Physics ***A314*** *(1979) 253*

[Fris33] R. Frisch and O. Stern,
Z. Phys. ***85****, (1933) 4*

[From94] F. Frommberger et al.,
Physics Letters ***B339*** *(1994) 17*

[Grun96] K. Gruner,
Diplomarbeit, Universitat Konstanz (1996), unpublished.

[Herm90] H. Herminghaus et al,
Proc. Linear Accelerator Conference (1990), Alberquerque

[HumT89] E. Hummel and J. A. Tjon,
Phys. Rev. Lett. ***63*** *(1989) 1788*

[Irel93] D.G. Ireland,
NIKHEF-K Electron Scattering Proposal PAC 1993

[Laco80] M. Lacombe et al.,
Phys. Rev. ***C21****, (1980) 861*

[Kasd97] W.J. Kasdorp,
Ph.D. Thesis, University of Utrecht (1997), unpublished.

[Mosc90] B. Mosconi, P. Ricci,
Nuclear Physics ***A517*** *(1990) 483*

[Munz96] G. Munoz,
Private Communication

[Munz97] G. Munoz,
Graduation Thesis, Universiteit Utrecht (1997)

[Nic93] National Instruments Corporation,
Labwindows User Manual, Version 2.3 (1993)

[Pow50] C. F. Powell,
Reports on Progress in Physics ***13*** *(1950), 350-424*

[Quin88] B.P. Quinn et al.,
Physics Review ***C37*** *(1988) 1609*

[Rabi40] I.I. Rabi, J.B. Kellog et al.,
Physics Review ***57*** *(1940), 677*

[Ruth11] E. Rutherford,
Phil. Mag., sixth series, ***21*** *(1911), 669*

[Ruth19] E. Rutherford,
Phil. Mag., sixth series, ***37*** *(1919), 537*

[Schi97] E. Schillings,
Graduation Thesis, Universiteit Utrecht (1997)

[Schr91] M. van der Schaar et al.,
Physical Review Letters ***66*** *(1991) 2855*

[Uden97] M. van Uden,
Ph.D. Thesis, NIKHEF (1997), unpublished.

[Vrie84] C. De Vries et al.,
Nuclear Instruments and Methods ***223*** *(1984) 1*

[Vrie90] L. De Vries et al.,
Nuclear Instruments and Methods ***292*** *(1990) 629*

[Witt93] P.K.A de Witt Huberts,
Nuclear Physics ***A553*** *(1993) 845c*

[Yuka35] H. Yukawa,
Proc. Phys. Math. Soc. Japan ***17*** *(1935) 48*